THESIS

THE IMPACT OF TROPICAL INTRASEASONAL VARIABILITY ON SUBSEASONAL-TO-SEASONAL PREDICTABILITY

Submitted by

Wei-Ting Hsiao

Department of Atmospheric Science

In partial fulfillment of the requirements

For the Degree of Master of Science

Colorado State University

Fort Collins, Colorado

Fall 2021

Master's Committee:

Advisor: Eric Maloney
Co-Advisor: Elizabeth Barnes

Nathan Mueller

ABSTRACT

THE IMPACT OF TROPICAL INTRASEASONAL VARIABILITY ON SUBSEASONAL-TO-SEASONAL PREDICTABILITY

Subseasonal-to-seasonal (S2S) timescales have been identified as a gap in weather forecast skill at 2 weeks to 2 months lead times. This timescale is set by midlatitude synoptic predictability limits, and sits between the typical weather timescale and the longer annual to interannual periods that may have skill due to knowledge of low-frequency phenomena such as El Niño-Southern Oscillation (ENSO). Previous studies have shown that tropical intraseasonal variability serves as an important source of S2S predictability in the midlatitudes based on a linear Rossby wave theory. The theory suggests that consistent weather patterns are excited by tropical divergence and associated teleconnections to the extratropics on S2S timescales that influence predictability. However, those physical processes that provide sources of S2S forecast skill have yet to be fully characterized. This thesis examines aspects of tropical intraseasonal variability that are important for S2S prediction, including how tropical intraseasonal variability has changed with warming over the last century and how the misrepresentation of such variability in a weather forecast model leads to errors in midlatitude precipitation S2S forecasts.

In the first part of this thesis, three reanalyses datasets (ERA5, MERRA-2, and ERA 20-C) are examined to quantify the amplitude changes in a dominant mode of intraseasonal tropical variability, the Madden-Julian oscillation (MJO), over the last century. MJO-associated precipitation and vertical velocity amplitude are found to exhibit a complex evolution over the observational record, where the precipitation has larger increases than the vertical velocity. A decrease in the ratio of MJO circulation to precipitation anomaly amplitude is detected over the observational period. Tropical weak temperature gradient theory is used to show that this decrease is consistent with the change in tropical dry static stability that has occurred under climate warming. The weakening MJO circulation per unit precipitation over the past century may have modified associated teleconnections and has implications for S2S prediction in the tropics and midlatitudes.

In the second part of the thesis, emphasis is placed on understanding S2S precipitation forecast errors for the western United States (U.S.) in an operational weather model. A set of hindcasts during boreal winter, where the tropics are nudged toward reanalysis, is compared to hindcasts without nudging. The western U.S. precipitation forecasts are found to improve with nudging at 3-4 week lead times. Using a multivariate k-means clustering method, hindcasts are grouped by their initial states and one cluster that exhibits an initially strong Aleutian Low is found to provide better forecast improvement. The improvement originates from the poor representation in the non-nudged hindcasts of the destructive interference between (1) the anomalous Aleutian Low and (2) the teleconnection pattern generated by certain phases of the MJO during non-cold ENSO conditions. These results suggest that improving the simulation of tropical intraseasonal precipitation during the early MJO phases under non-cold ENSO may lead to better 3-4 week precipitation forecasts in the western U.S.

TABLE OF CONTENTS

CHAPTER 1

Introduction

Accurate weather prediction is beneficial to human society. For example, the cost related to weather and climate disasters was over 47 billion U.S. dollars annually on average between 1981-2020 (National Centers for Environmental Information; accessed in August 2021), and having accurate weather prediction may allow humans to better prepare for such disasters and reduce the loss to property and human life. Weather forecasts on shorter timescales within a week have relatively good skill based on the chaotic nature of the atmosphere and the good understanding of atmospheric physical processes (Bauer et al. 2015). The forecast skill on longer timescales of more than 30 days is also attainable because it depends on well-understood slowly-varying lower boundary conditions such as sea surface temperature (Chen et al. 2010; Doblas-Reyes et al. 2013) and processes related to them such as El Niño-Southern Oscillation (ENSO). However, current weather forecast systems have difficulty providing good forecasts on timescales of about 10 to 30 days (Hudson et al. 2011), and the processes regulating predictability on these timescales are not well understood. These so-called subseasonal-to-seasonal (S2S) timescales have long been identified as a gap zone of weather forecast skill even though skillful forecasts at these ranges are highly desired by society (White et al. 2017).

Tropical intraseasonal variability is thought to be an important source of S2S predictability (e.g. Vitart et al. 2012). In the tropics, regions of precipitation are commonly associated with vertical air motion and divergence at the upper troposphere. Based on a linear Rossby wave theory, when such divergence occurs and a divergent flow impinges on a strong positive meridional absolute vorticity gradient (for example, in the subtropical jets), vortex stretching and vorticity advection can generate a Rossby wave source (RWS), exciting stationary Rossby wave trains to the extratropics (Hoskins and Karoly 1981; Sardeshmukh and Hoskins 1988; Hoskins and Ambrizzi 1993). Tropical variability that evolves slowly on S2S timescales, such as the Madden-Julian oscillation (MJO; Madden and Julian 1971, 1972), causes tropical convection to be in a similar state for a week or longer which excites associated RWS and consistent midlatitude teleconnections (Tseng et al. 2019). These teleconnections propagate into the midlatitudes 1-2 weeks after tropical RWS appears (Branstator 2014) and generate consistent weather patterns. Based on the physical process discussed, tropical intraseasonal variability could be seen as a source of S2S predictability.

As discussed, tropical convection is able to excite consistent weather patterns in the extratropics (Tseng et al. 2019). Hence, how tropical intraseasonal variability is affected by a changing climate can have important implications for tropical-extratropical interaction, S2S predictability, and future weather forecasts. A dominant mode of tropical intraseasonal variability that affects S2S predictions, the MJO (Madden and Julian 1971, 1972), is thought to be strongly impacted by a warming climate (Maloney et al. 2019). In Chapter 2, we investigate changes in the MJO over the observational record using three reanalysis datasets. The ratio of MJO circulation to precipitation amplitude is found to have decreased over the past few decades, and such a trend can be explained by the increase in tropical dry static stability in the troposphere as the climate warms. In isolation, this result implies that the MJO has become increasingly inefficient at exciting the teleconnection patterns bridging the tropics and the extratropics. If changes to the basic state vorticity gradients that affect generation of the RWS and teleconnection pathways are not considered, this may decrease S2S predictability in the extratropics. This work is published in *Geophysical Research Letters* as:

- Hsiao, W.-T., Maloney, E. D., & Barnes, E. A. (2020). Investigating Recent Changes in MJO Precipitation and Circulation in Multiple Reanalyses. *Geophysical Research Letters*, *47*(22), e2020GL090139.

Since tropical-extratropical interactions excited by tropical intraseasonal variability is a source of prediction skill on S2S timescales (Vitart et al. 2012), it is possible that misrepresentation of the tropics in models could lead to forecast errors in the extratropics. To improve current weather forecasts on S2S timescales in operational weather models, one way is to determine how and why tropical forecast errors can lead to large degradation in extratropical S2S forecast skill. In Chapter 3, hindcasts with the tropics nudged toward the observational fields (Dias et al. 2021) are analyzed to identify the tropical origins of forecast errors, particularly those in the western United States (U.S.) precipitation. Conditional forecast improvements are identified by subsetting the hindcasts using a multivariate k-means clustering method. One subset of hindcasts with the greatest forecast improvements suggests a particular physical process that is not simulated well due to a poor model simulation of the MJO. This work will be submitted to *Geophysical Research Letters* as:

- Hsiao, W.-T., Barnes, E. A., Maloney, E. D., Tulich, S. N., Dias, J., and Kiladis G. N. (2021). Role of the tropics and its extratropical teleconnections in state-dependent improvements of UFS precipitation forecasts. *To be submitted.*

Finally, a summary of this thesis and future perspectives are provided in Chapter 4.

CHAPTER 2

Investigating Recent Changes in MJO Precipitation and Circulation in Multiple Reanalyses[1]

2.1 Introduction

The Madden-Julian oscillation (MJO; Madden and Julian 1971, 1972) is the dominant mode of large-scale tropical precipitation variability on intraseasonal timescales. MJO activity impacts the occurrence of extreme weather events not only in tropics but also at higher latitudes due to its remote teleconnections (Zhang 2013). Because of its ability to modulate weather across the globe, with clear implications for lives and property, extensive research is being conducted about the MJO, with increasing attention given to the evolution of the MJO under anthropogenic warming (Maloney et al. 2019). As global temperatures rise, MJO activity is expected to be impacted by competing effects, making the projections of the MJO difficult. For example, an increased basic state vertical moisture gradient in the lower troposphere increases the efficiency with which vertical motion moistens the atmosphere, leading to a strengthening of MJO-associated convection (Arnold et al. 2013; Holloway and Neelin 2009). In contrast, an increased dry static stability decreases the efficiency by which diabatic heating induces vertical motion (Knutson and Manabe 1995; Sherwood and Nishant 2015; Sobel and Bretherton 2000), which would tend to weaken MJO-associated convection (e.g. Chikira 2014). Future projections from most global climate models (GCMs) suggest an increase in the amplitude of MJO precipitation under anthropogenic warming, although MJO circulation anomalies weaken, or at least increase less than

[1] This section contains material that is published in *Geophysical Research Letters* as:
Hsiao, W.-T., Maloney, E. D., & Barnes, E. A. (2020). Investigating Recent Changes in MJO Precipitation and Circulation in Multiple Reanalyses. *Geophysical Research Letters*, *47*(22), e2020GL090139.

precipitation (Maloney et al. 2019). Analysis of the reconstructed historical record from instrumental observations and reanalysis shows positive trends of MJO amplitude over the 20th century in surface pressure and precipitation (Oliver and Thompson 2012) and in the late 20th century in zonal winds (Jones and Carvalho 2006; Slingo et al. 1999). However, other studies have found no trend in boreal wintertime MJO amplitude from the 1980s to the 2000s when using an outgoing longwave radiation-related metric (Tao et al. 2015).

Recent evidence suggests that the MJO may undergo structural changes with warming and differences in intensification rate in its associated precipitation and circulation components. Such changes would be important because teleconnections generated by upper level divergence associated with MJO convection have a large impact on extratropical weather and its predictability (Ferranti et al. 1990; Zhang 2013). Instead of examining the amplitude of the MJO with a single variable, Maloney and Xie (2013) and Wolding and Maloney (2015) suggest that in the deep tropics where the weak temperature gradient (WTG) approximation holds (Sobel and Bretherton 2000), the amplitude ratio of vertical velocity to precipitation associated with the MJO is constrained by dry static stability. Since the temperature profile in the free tropical troposphere roughly follows a moist adiabat determined by convective adjustment in tropical convecting regions (Knutson and Manabe 1995), the dry static stability profile may be constrained by future sea-surface temperature (SST) warming, thus providing a constraint on future MJO behavior.

A recent study found that the ratio of MJO-associated circulation to precipitation amplitude follows WTG balance in anthropogenic warming simulations (Bui and Maloney 2019). The WTG approximation can be applied to the thermodynamic equation to produce the following approximate balance in the tropical free troposphere, where horizontal temperature gradients are small (Sobel and Bretherton 2000),

$$\omega \frac{\partial s}{\partial p} \approx Q_1 \tag{2.1}$$

where ω is the vertical pressure velocity, s the dry static energy (DSE), and Q_1 the apparent heat source (Yanai et al. 1973). Note that all variables represent the large-scale area average. If it is further assumed that precipitation is proportional to Q_1 in MJO convective regions, and that the vertical structure of Q_1 is not changed (Maloney and Xie 2013), it follows that at a given level,

$$\Delta\left(\frac{\omega}{P}\right) \propto \Delta\left(\frac{\partial s}{\partial p}^{-1}\right) \tag{2.2}$$

where P is the surface precipitation rate and Δ denotes the relative change from a reference state to a new state. Bui and Maloney (2019) examined GCM simulations forced by Representative Concentration Pathway 8.5 (RCP8.5) in a subset of models participating in the Coupled Model Intercomparison Project 5 (CMIP5) that simulated realistic MJOs. While the amplitude changes of MJO precipitation and vertical velocity were individually not detectable until 2080, the ratio of MJO vertical velocity to precipitation amplitude showed detectable decreases as early as 2021–2040. Consistent with WTG balance and the proportionality of precipitation to Q_1, the ratio of MJO vertical velocity to precipitation amplitude matches the change in dry static stability in the simulations, implying that this theory could explain and predict the evolution of the MJO, even in the observational record that has exhibited warming.

Following this work, we investigate the temporal evolution of MJO-related precipitation and circulation amplitude and their ratio in two reanalyses (ERA5 and MERRA-2) to assess whether changes to the MJO can be detected in recent decades. A similar analysis is also applied on a century-long reanalysis (ERA-20C) to further support findings over the past few decades and to assess recent changes to the MJO in the context of low-frequency variability. Our purpose is to determine whether WTG balance can explain changes in MJO activity in the real world, which could help support projections of MJO under continued anthropogenic warming.

2.2 Data and Methodology

Two reanalysis data sets spanning 1981–2018 are employed to assess changes in MJO amplitude and the background environment in recent decades. The Modern-Era Retrospective analysis for Research and Applications version 2 (MERRA-2; Gelaro et al. 2017) and the European Centre for Medium-Range Weather Forecasts (ECMWF) reanalysis (ERA5; Hersbach et al. 2020) are the main data sets used to investigate MJO activity in recent decades. The ECMWF 20th century reanalysis (ERA-20C; Poli et al. 2016) is used to evaluate long-term changes in MJO behavior over 1901–2009. The MERRA-2, ERA5, and ERA-20C data sets have spatial (temporal) resolutions of 0.5° × 0.625° (3 hours), 0.25° × 0.25° (1 hour), and spectral truncation of T159 (1 hour), respectively. For the purpose of investigating large-scale dynamics, all variables are regridded to have a common horizontal spatial resolution of 2.5° × 2.5°. Vertical pressure velocity and precipitation are averaged into daily means, and temperature and DSE are originally obtained as monthly means. Wolding and Maloney (2015) imply that for good approximation, the slowly varying background DSE gradient is appropriate to use in **Equation 2.1** for determining the dominant WTG MJO balance. While the precipitation data in both reanalyses is model-generated and comes with substantial caveats, inhomogeneities in satellite-observed precipitation over the tropics make it difficult to use to detect climate trends (e.g. Yin et al. 2004). Furthermore, the moisture budget in the reanalyses products is more internally consistent, and thus, we focus on reanalysis precipitation for this work.

For ERA5 and MERRA-2, MJO activity is assessed by its associated precipitation and vertical pressure velocity amplitudes, with vertical pressure velocity at 400 hPa (ω_{400}) used given the top-heavy nature of convection in the MJO (Kiladis et al. 2005). Specifically, the occurrence of an MJO event is defined as when the magnitude of the outgoing longwave radiation-based MJO index (OMI; downloaded from NOAA PSL website; see Kiladis et al. 2014, for definition) exceeds 1.0. Note that we split our analysis into 19-year periods, and so OMI is normalized within each time period (as in Bui and Maloney 2019) to reflect possible changes in variance of outgoing longwave radiation fields. Boreal winter (November to April) MJO composites for each of its eight phases are then generated for 30- to 90-day bandpass filtered variables as is commonly done in the MJO literature (e.g. Kiladis et al. 2014). Amplitudes of MJO precipitation and ω_{400} for each location are calculated as the root mean square values across the composites of the eight MJO phases.

Since OMI is defined by satellite OLR fields that are not available prior to 1979, MJO activity in ERA-20C is assessed using the standard deviations of precipitation and ω_{400} in the MJO band. The MJO band is defined by bandpass filtering fields to frequencies of 30–90 days and zonal wavenumbers of 1–5.

Boreal winter averages derived from monthly means of temperature and DSE are used to assess the background environment changes that could impact MJO activity. Dry static stability at 400 hPa is computed using the vertical gradient of DSE between 350 and 450 hPa.

Our focus is on the time evolution of the amplitudes of MJO precipitation and ω_{400} in the Indo-Pacific warm pool region (the IPWP region; 15°S to 15°N, 60°E to 180°) where the MJO is most active, as shown in the boxed region in **Figure 2.1**. Area-averaged MJO precipitation and ω_{400} amplitudes over the IPWP region are used as metrics to quantify overall MJO activity.

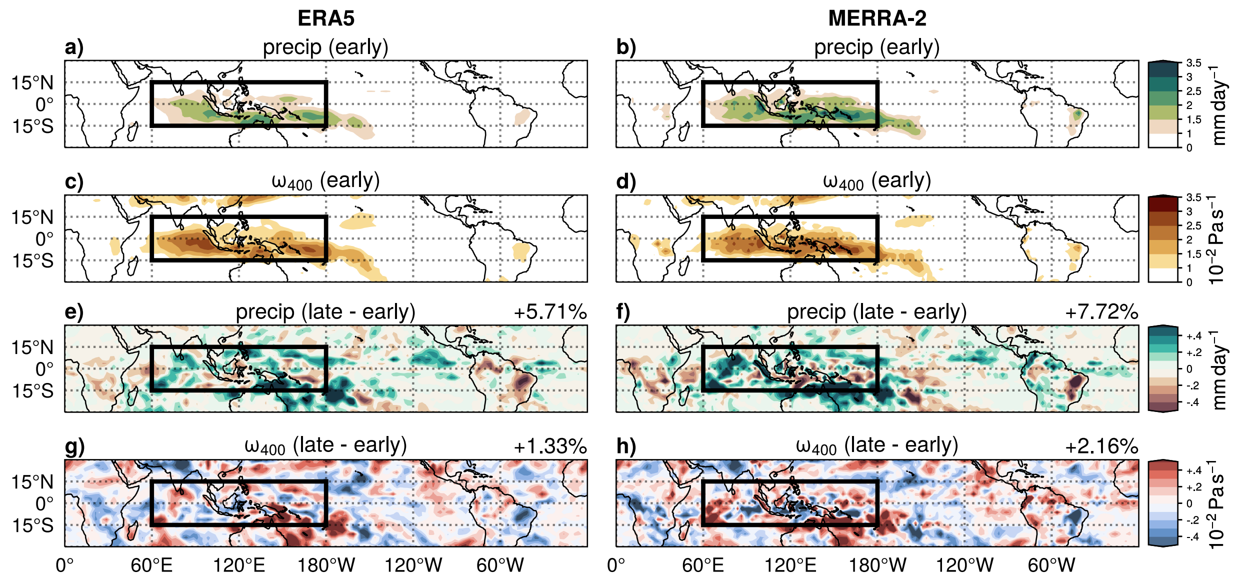

Figure 2.1. The boreal winter composite amplitudes of (a, b) MJO precipitation and (c, d) MJO ω_{400} during the early period (1981–1999) and (e–h) their difference from the late period (2000–2018), from (left column) ERA5 and (right column) MERRA-2. The black rectangle encloses the Indo-Pacific warm pool region, and the percentage values shown in the upper right corners of (e–h) are the area-averaged relative changes over the region.

Composites obtained from 19-year running windows are extensively used in this study, similar to the averaging window length of 20 years used in Bui and Maloney (2019). This window length is chosen to reduce noise from decadal variations, but also to retain enough data points to show the time evolution of MJO activity. Since the entire time period analyzed is 38 years in ERA5 and MERRA-2, the first and the last 19 years of the record are the only two periods that are truly independent, and we refer to these as the early period (1981–1999) and the late period (2000–2018). The conclusions in this study are not sensitive to the choice of window length used between 15 and 25 years (**Figure A2.1**).

Relative change (Δ) in percent is the main metric used to define changes in this study. Specifically, for any quantity X, the relative change compared to its reference state (X_{ref}) is defined by

$$\Delta(X) = \frac{X - X_{ref}}{X_{ref}} \cdot 100\% \tag{2.3}$$

where X_{ref} denotes the quantity over the early period (1981–1999).

2.3 Results

First, we explore the spatial structure of MJO activity in the two reanalyses. The amplitude of MJO precipitation and ω_{400} maximize in the IPWP region (**Figures 2.1a–2.1d**) in both reanalyses during the early period. The changes in MJO precipitation and ω_{400} amplitude between the late period and the early period have rich spatial structures, which are similar between the reanalyses (**Figures 2.1e–2.1h**). Increases in both amplitudes occur to the south of India, at the southern edge of the Pacific warm pool, and near the Philippines. Decreases in both amplitudes occur near 5°S over the Maritime Continent. The regions of large amplitude of the MJO do not change substantially between the early and late period, allowing us to assess the temporal change in MJO activity within the IPWP region. The area-averaged amplitude of MJO precipitation and ω_{400} in the IPWP region both show increases in the late period relative to the early period with precipitation intensifying by 5.6% in ERA5 and 7.6% in MERRA-2 and ω_{400} intensifying by 1.2% in ERA5 and 2.1% in MERRA-2. Most important for this study, MJO precipitation amplitude intensifies more than MJO ω_{400} amplitude in both reanalyses, although MJO activity in MERRA-2 is strengthened slightly more than in ERA5.

The 19-year running area-averaged MJO precipitation and ω_{400} amplitude in the IPWP region increase between the early and the late periods of the record, while the amplitudes in MERRA-2 exhibit larger changes than those in ERA5. However, both reanalyses demonstrate qualitatively similar fluctuations in between: in the early 1990s, both of the amplitudes rise quickly, followed by a plateau and then a slight decrease afterward (**Figures 2.2a** and **2.2b**). The strengthening of the boreal wintertime MJO activity during the late 20th century is consistent with previous studies examining observed zonal wind changes at 200 and 850 hPa (Jones and Carvalho 2006). Moreover, both reanalyses agree that throughout most of the record, MJO precipitation amplitude shows larger positive changes than MJO ω_{400} amplitude.

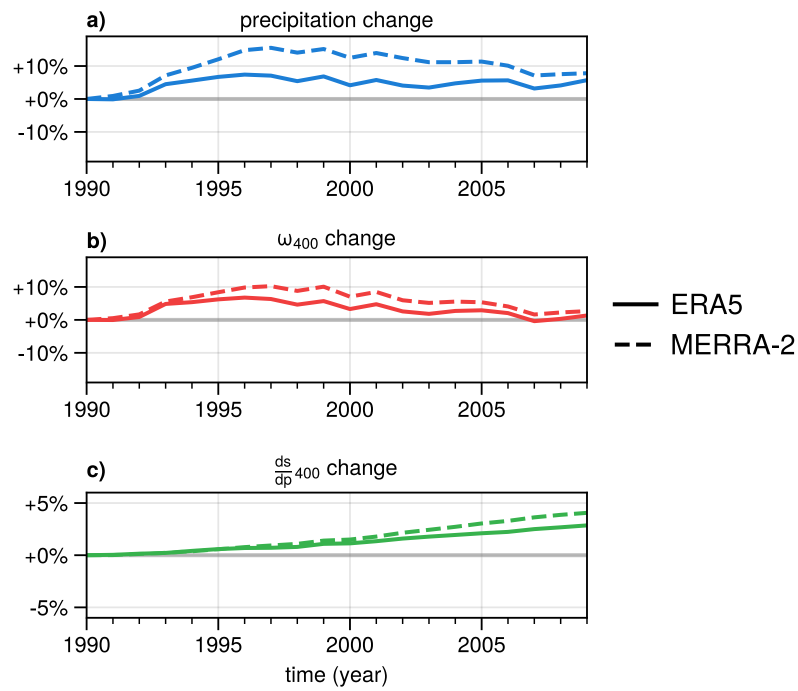

Figure 2.2. Relative change in 19-year wintertime running composites of (a) MJO precipitation amplitude, (b) MJO ω_{400} amplitude, and (c) dry static stability at 400 hPa with respect to the early period. The x axis denotes the central years of the associated time window, for example, 2000 denotes the period of 1991–2009. The y axis denotes the relative change to the early period.

While we attempted to explain the fluctuating pattern in MJO precipitation and ω_{400} amplitude, we could find no obvious connections between them and interannual to decadal variability in surface air temperature. The evolution of surface air temperature in the IPWP region (**Figure A2.2b**) and its evolution relative to the whole tropics (**Figure A2.2c**) do not resemble the variability in the MJO amplitude time series, which have different trends from the early 1990s onward (**Figures 2.2a** and **2.2b**). Commonly used Pacific SST indices that capture interannual to decadal variability also do not show similar variability to the MJO amplitude time series (cf. **Figures 2.2a** and **2.2b** with **Figure A2.3** SST indices).

To sum up, both MJO precipitation and ω_{400} amplitude increase from the early period to the late period in the IPWP region in both reanalyses, although the time evolution is non-monotonic and the amplitude of the change varies between the reanalyses. The time series of the amplitudes are not easily explained by tropical SST variability. However, a robust result common among different time periods and reanalyses is that the increase in MJO precipitation amplitude is always stronger than in MJO ω_{400} amplitude, consistent with what WTG balance would predict based on the increasing tropical static stability with SST warming observed in recent decades (**Figure 2.2c**; see also e.g. Sherwood and Nishant 2015). We explore this contention more below.

Given a change in dry static stability, the theoretical change in the ratio of MJO ω_{400} to precipitation amplitude can be computed if one assumes that WTG balance holds (**Equation 2.1**) and that the vertical structure of Q_1 associated with the MJO is not changed (**Equation 2.2**). Previous modeling studies have shown good agreement between static stability changes and this ratio when applied to MJO-associated wind and precipitation variance (Bui and Maloney 2018; Maloney and Xie 2013; Wolding et al. 2016; Wolding and Maloney 2015). As the climate system warms, tropical dry static stability increases in the troposphere because the atmospheric profile in the deep tropics roughly follows a moist adiabat set by the surface temperature in convecting regions (Knutson and Manabe 1995). Consistently, increasing dry static stability has been observed in recent years as surface temperature has increased (Allen and Sherwood 2008). Because surface temperature has increased since 1981 (**Figure A2.2a**), **Equation 2.2** would argue for a greater change in MJO precipitation amplitude compared to MJO ω_{400} amplitude.

Figures 2.3a and **2.3b** display the temporal evolution of the inverse of dry static stability and the ratio of MJO ω_{400} to precipitation amplitude (MJO ω_{400}/P; see **Equation 2.2**) in ERA5 and MERRA-2. The gray diagonal line denotes the predicted theoretical relationship between MJO ω_{400}/P and inverse static stability assuming WTG theory holds and the vertical structure of the MJO remains unchanged. Between the late period and the early period (the two outlined endpoints), the decrease of the inverse of dry static stability is 2.8% in ERA5 and 4.0% in MERRA-2, and the decrease of MJO ω_{400}/P is 4.2% in ERA5 and 4.9% in MERRA-2. Consistent with WTG theory, MJO ω_{400}/P and the inverse of dry static stability show comparable decreases between the early period (1981–1999) and the late period (2000–2018). Agreement is also good in ERA5 for interim periods, especially until about 2000 (**Figure 2.3a**). Considering the complicated temporal evolution of MJO precipitation and ω_{400} amplitude (**Figure 2.2**), WTG balance provides a reasonable explanation for the evolution of MJO ω_{400}/P over the past 38 years, especially when considering the start and end of the record.

As many MJO studies use zonal wind amplitude as a metric of MJO activity (e.g. Jones and Carvalho 2006; Slingo et al. 1999), we also examine the amplitude of MJO 850-hPa zonal wind (u_{850}) for reference. The evolution of the ratio of MJO circulation to precipitation amplitude is defined here using u_{850} (MJO u_{850}/P). Although using u_{850} is not a direct application of WTG balance in **Equation 2.2**, the amplitude of horizontal velocity should scale with vertical velocity through divergence if the vertical structure doesn't change (Maloney and Xie 2013). Under such conditions, we would expect a qualitatively similar decrease in the ratio of MJO u_{850} to precipitation amplitude. **Figure A2.4** shows that u_{850} amplitude relative to precipitation does decrease in a qualitatively similar way, although with stronger decreases relative to P than for ω_{400}.

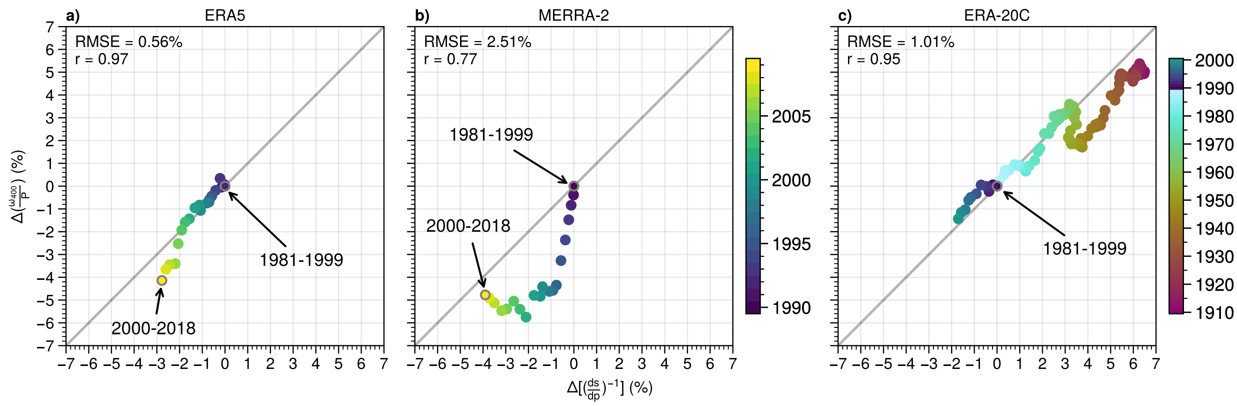

Figure 2.3. Relative change in (x axis) the reciprocal of dry static stability at 400 hPa and (y axis) the ratio of MJO ω_{400} to precipitation amplitude over the IPWP region between 19-year running windows and the early period. Colors indicate the central year of the running window. The gray diagonal line denotes the change in the ratio predicted by WTG balance assuming vertical heating structure is unchanged (**Equation 2.2**). Root mean square errors (RMSEs) of MJO ω_{400}/P relative to theoretical predictions are provided in each panel. Correlation coefficients (r) between the two variables are also provided to show how coherent they change. Note that the MJO-associated quantities are defined using OMI for (a) ERA5 and (b) MERRA-2, whereas standard deviations in the MJO wavenumber-frequency band are used for (c) ERA-20C.

Although MJO ω_{400}/P generally follows the change in the inverse of dry static stability, there exist deviations from theoretical predictions, with maximum differences of about 1.5% in ERA5 and 4% in MERRA-2. To place these values in a larger-scale context, we compare **Figures 2.3a** and **2.3b** to **Figure 2.3c** that shows results from ERA-20C spanning 1901–2009. The theoretical estimate works well in ERA-20C over the whole century, with about 7–8% decreases in both MJO ω_{400}/P and inverse static stability over the century. The maximum deviation of MJO ω_{400}/P change in ERA-20C is about 2% from theoretical values predicted by the inverse of dry static stability. Deviations of ERA5 from theoretical values are even smaller than this, while deviations in MERRA-2 are larger. As described below, deviations of MERRA-2 from the theoretical estimate may occur due to the imperfect assumption of proportionality of Q_1 at 400 hPa and P.

In MERRA-2, **Equation 2.2** overestimates the decrease in MJO ω_{400}/P in the intervening periods but works well for the two endpoints. MJO ω_{400}/P in MERRA-2 shows stronger decreases than ERA5 during the interim period largely because it has a larger P amplitude change than ERA5. The exact reasons for differences between the two analyses are unclear, although they may depend on the different behavior of tropical convection simulated by the two reanalysis models. The differing DSE profile changes between ERA5 and MERRA-2 for the IPWP region (**Figure A2.5**) not only indicate differing static stability changes but also circumstantially suggest different changes to the convective heating structure between data sets given the regulation of tropical tropospheric temperature by convective heating. Such structure changes would affect how well the balance in **Equation 2.2** reflects **Equation 2.1**, considering the assumption about the proportionality of P to Q_1 at 400 hPa. MERRA-2 exhibits more warming in the lower troposphere than ERA5, presumably associated with increased condensational heating and precipitation generation there, which would produce greater decreases in MJO ω_{400}/P than that expected by looking at the 400 hPa level in isolation. The rate of increase in low-level warming in MERRA-2 is particularly strong until the 19-year period centered on 1997, possibly consistent with the greater MJO precipitation amplitude increase in MERRA-2 during that time than ERA5 (**Figure 2.2**), although translating mean state convective structure changes to those on subseasonal timescales should be done with care.

An examination of MJO anomaly amplitudes of Q_1 at 400 hPa and precipitation suggests a weaker consistency between the two quantities in MERRA-2 (**Figure A2.6**), consistent with possible vertical structure changes. However, while the change in the ratio of ω_{400} to Q_1 amplitude at 400 hPa generally follows dry static stability in ERA5, the agreement is not as good as in

MERRA-2 (**Figure A2.7**), which might also explain some of the differing behavior in **Figure 2.3**. The reasons for this discrepancy are unclear.

2.4 Summary

The changes to MJO precipitation and ω_{400} amplitude from 1981 to 2018 are examined in three reanalysis data sets: ERA5, MERRA-2, and ERA-20C. Both amplitudes in ERA5 and MERRA-2 individually increased from the early period (1981–1999) to the late period (2000–2018) (**Figure 2.1**). However, their temporal behavior is non-monotonic in that both amplitudes intensify from 1981 to 1997 and slowly weaken or remain constant thereafter (**Figures 2.2a** and **2.2b**). Interannual-to-decadal surface temperature variability (**Figures A2.2** and **A2.3**) shows no simple relationship with this non-monotonic behavior in MJO activity changes.

When viewed together, amplitude changes of MJO precipitation are larger than MJO ω_{400} throughout the past four decades relative to the early period (1981–1999). A preferential strengthening of MJO precipitation amplitude relative to MJO ω_{400} amplitude is predicted by WTG balance with a warming climate, in that increasing dry static stability in response to SST warming in recent decades makes vertical motion more efficient at compensating latent heat release in deep convective regions. The fractional amplitude changes in the ratio of MJO ω_{400} to precipitation between 1981–1999 and 2000–2018 approximately match inverse dry static stability changes with climate warming, consistent with WTG balance (**Figures 2.3a** and **2.3b**). A similar result is shown in ERA-20C between 1901–1919 and 1991–2009 (**Figure 2.3c**).

While trends in these reanalyses appear to generally follow WTG balance, differences exist in the behavior of the three reanalyses. MJO precipitation and ω_{400} amplitude increases are larger in MERRA-2 than in ERA5, especially in intermediate periods between the beginning and end of the record, although they show qualitatively similar time series variability (**Figure 2.2**). Decreases in MJO ω_{400}/P also fit the theoretical prediction based on the inverse of dry static stability better in ERA5 and ERA-20C than in MERRA-2 across all 19-year periods examined in terms of RMSE, and these differences may be associated with differences in the simulated structure of tropical deep convection, which remains a topic for further investigation.

The present paper provides a preliminary assessment of MJO activity changes in precipitation and vertical velocity over the past four decades that include both anthropogenic forcing and natural variability and uses a century-long data set to assess recent changes in the context of natural variability over the longer record. Our results based on observations support those previously derived from climate models (e.g. Bui and Maloney 2019) suggesting that decreases in MJO ω_{400}/P occur as surface temperatures warm due to anthropogenic forcing. Nevertheless, discrepancies between results from ERA5 and MERRA-2 leave lingering questions about the degree to which changes to the MJO can be explained by WTG theory, including the assumption that Q_1 has no vertical structural changes in response to climate warming. Further work using a broader set of observational data including tropical sounding and other in situ records is needed to affirm the validity of **Equation 2.2** for explaining MJO behavior.

CHAPTER 3

Role of the Tropics and its Extratropical Teleconnections in State-Dependent Improvements of UFS Precipitation Forecasts[2]

3.1 Introduction

Extended-range (11-30 day) and subseasonal-to-seasonal (S2S) predictability in the extratropics has been shown to partially originate in the tropics (Robertson et al. 2015). One source of predictability is provided by tropical-extratropical teleconnections that can emerge approximately one week after being excited by a Rossby wave source in the subtropics, which is ultimately generated by upper-tropospheric tropical divergence associated with convection (Branstator 2014; Hoskins and Ambrizzi 1993). This mechanism has been established theoretically using linear Rossby wave theory (Hoskins and Karoly 1981; Sardeshmukh and Hoskins 1988), and its implications for S2S predictability have been investigated largely using conditional analysis from observations (e.g. Hendon et al. 2000; Matthews et al. 2004) and from weather model output (e.g. Ferranti et al. 1990; Vitart and Molteni 2010). Exploring tropical sources of S2S predictability in operational weather forecast models may not only further provide insights into the mechanisms underlying this predictability, but may also provide model developers and forecast agencies information on when forecasts are more or less reliable, and which parts of the model to improve to engender further forecast gains.

To investigate the tropical origins of global extended-range forecast skill during boreal winter and associated errors that can degrade forecast skill in the operational forecast system, a set

[2] This section contains material that is to be submitted to *Geophysical Research Letters* as:
Hsiao, W.-T., Barnes, E. A., Maloney, E. D., Dias, J., Tulich, S. N., & Kiladis, G. N. (2021). Role of the tropics and its extratropical teleconnections in state-dependent improvements of UFS precipitation forecasts. *To be submitted*.

of hindcasts were performed by Dias et al. (2021). Hindcasts over a twenty-year period were run with the tropics nudged toward reanalysis in an operational weather forecast model from the Unified Forecast System (UFS) developed by the National Oceanic and Atmospheric Administration (NOAA). Their results showed that with corrected representations of *tropical* winds, mass, temperature, and humidity fields, forecasts of precipitation and 500 hPa geopotential height (z500) are significantly improved in the Northern Hemisphere extratropics at 2-4 week lead times. Notably, they also showed that forecast improvements due to tropical nudging are dependent on the initial state. For example, hindcasts are improved relatively more at four-week leads in the Northern Hemisphere extratropics with nudging when the Madden-Julian oscillation (MJO; Madden and Julian 1971, 1972) is active at initialization.

Since tropical heating, such as that generated by the MJO, is capable of exciting detectable and consistent teleconnection patterns in the extratropics (e.g. Ferranti et al. 1990; Matthews et al. 2004; Tseng et al. 2019), it is likely that extratropical forecasts in certain regions will be improved by correcting errors in the forecasted tropical heating, as has been suggested by previous studies (Ferranti et al. 1990; Bielli et al. 2010; Jung et al. 2010). Here, we investigate the specific initial states that lead to extratropical forecast improvements in the tropical nudging experiments described by Dias et al. (2021). Specifically, we condition forecast improvements of precipitation in Western United States (U.S.) by their initial states using a multivariate clustering procedure, which will be shown to capture the underlying physical mechanism more cleanly when compared to conditioning on conventional climate indices. This approach allows us to investigate the initial states associated with better forecast improvement due to the tropical nudging without *a priori* assumptions of the exact physical phenomena associated with the improvements. We demonstrate that one cluster of hindcasts with a particular initial state shows greater forecast improvement than the others, and we scrutinize the mechanisms associated with this improvement due to tropical nudging.

3.2 Methodology

3.2.1 Model and Experimental Setup

Here, we utilize the hindcasts conducted by Dias et al. (2021) using a leading U.S. forecast model, specifically, version 15.1.1 of the NOAA/ National Centers for Environmental Prediction Global Forecast System (NOAA/NCEP GFS v15.1.1). Three sets of simulations are conducted and are described below. For details of the model configuration, see **Appendix A** and Dias et al. (2021).

In the first set of hindcasts, ***REPLAY***, a good approximation of the observed state is produced. The incremental analysis update (IAU; Bloom et al. 1996) scheme is utilized to nudge zonal and meridional winds, mass, temperature, and specific humidity over the whole globe toward the observed states (represented by ERA-Interim reanalysis; Dee et al. 2011) during November 1999 to April 2018 for the extended boreal winter (November to April).

A second set of hindcasts, ***FREE***, are performed to evaluate the forecast performance of the model in free-running mode (i.e. with no nudging). In this setting, the model is run freely out to 30 days in each hindcast, where hindcasts are initialized every five days from the states in REPLAY.

A third set of hindcasts, ***NUDGE***, are performed to assess the effect on S2S forecast performance in the extratropics when the tropics are represented accurately. The design of NUDGE is the same as FREE, except that the nudging method used in REPLAY is applied within 30°S-30°N using a weighting function that is unity between 10°S-10°N and is reduced to zero toward 30°N and 30°S (the same form of nudging is used in Jung et al. 2010; and Dias et al. 2021).

3.2.2 Quantifying forecast performance of the western U.S. precipitation

The present study puts emphasis on the forecast performance of precipitation along the U.S. West Coast, which is assessed by its grid-wise area-averaged mean absolute error (MAE) over the region 30°N-50°N, 120°W-140°W (referred to as the **western U.S.**; the box in the **Figure 3.1** map) in FREE or NUDGE compared to REPLAY. The improvement produced by NUDGE is quantified by the difference between the MAE of FREE and NUDGE. The precise bounds of the western U.S. spatial averaging domain do not affect our conclusions (not shown).

A multivariate k-means clustering analysis is performed to subset the hindcasts by their initial states. After assigning the number of desired clusters, k-means clustering partitions the data in a feature space by minimizing the within-cluster variance (Lloyd 1982). This k-means clustering approach allows us to investigate the initial states associated with better forecast improvement due to tropical nudging, without *a priori* assumption of the exact physical phenomena associated with the improvement. The data are processed in the following way before being input into the cluster analysis: (1) anomalies are calculated by subtracting daily climatologies from the fields of interest, where lead-dependent climatologies are used for the hindcasts; (2) empirical orthogonal functions (EOFs; Lorenz 1956) of 20°S-90°N and 60°E-90°W precipitation and 200 hPa zonal wind (u200) anomalies are computed based on the uncentered covariance matrices of each variable; (3) the dimensionless principal components (PCs) of all of the EOFs are weighted by their variance explained; (4) the weighted PCs from the two variables are stacked to form a feature vector which is used as input to the k-means clustering algorithm. The choice of using u200 and precipitation to define unique characteristics of the initial states is motivated by their importance for representing the tropical forcing pattern (i.e. precipitation) and the basic state winds that can impact tropical-extratropical teleconnections (i.e. u200). We implement the k-means clustering algorithm by *scikit-learn* v0.23.2 (Pedregosa et al. 2011) with the default settings except for K = 8 (i.e. 8 clusters) and setting the initialization seed to 0. We note, however, that similar conclusions hold for K = 8 to 10 and with four random initialization seeds (0, 1, 2, and 3 as integers) for each K (not shown). Values of K below 8 did not identify clusters with robust improvement in forecast performance, while K larger than 10 identified similar forecast improvements, but the small sample sizes of the clusters was not as desirable.

To associate the clusters with known modes of climate variability, we also use metrics that represent the states of the MJO and El Niño-Southern Oscillation (ENSO). The outgoing longwave radiation MJO index (OMI; Kiladis et al. 2014) is used to assess the intensity of the MJO and its phases, where an MJO event is defined as when the magnitude of OMI ≥ 1. The multivariate ENSO Index Version 2 (MEIv2; Zhang et al. 2019) is used to quantify ENSO states.

3.3 Results

Nudging in the tropics generally improves the Week 3-4 (days 15-28) precipitation forecast performance in the western U.S. with the distribution of the MAE shifted toward zero in NUDGE compared to FREE (**Figure 3.1**). The peak of the MAE distribution is reduced by about 1 mm day^{-1} in NUDGE, while the average and the median are reduced by 0.67 and 0.68 mm day^{-1}, respectively. Improvements in NUDGE relative to FREE emerge primarily during Week 3, shown by the right tails of the weekly distribution of MAE reduction (**Figure A3.1**), suggesting that S2S timescale processes are relevant for the improvement. Overall, nudging improves the forecast performance in the western U.S., particularly for cases in FREE that are relatively poor in the Week 3-4 range (**Figure A3.2**), as also discussed by Dias et al. (2021).

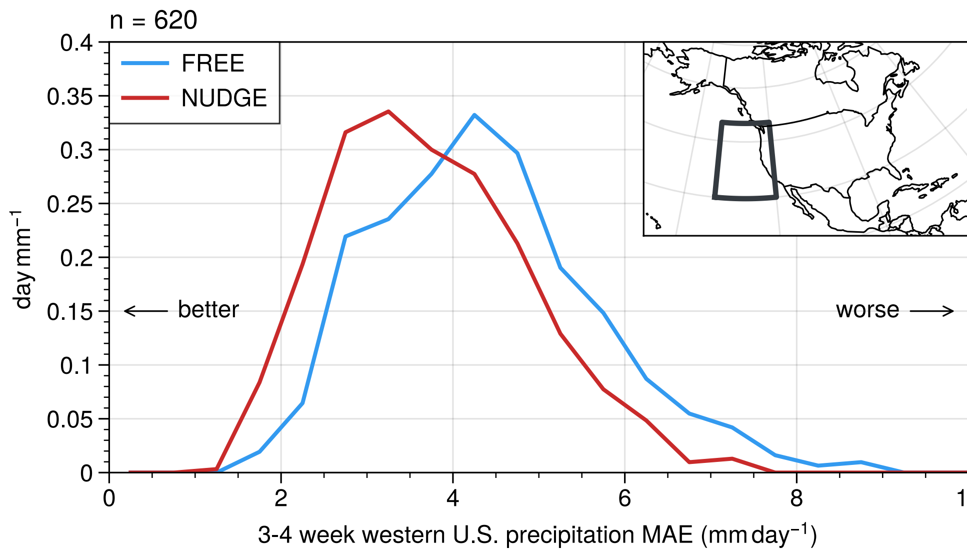

Figure 3.1. The distribution of the western U.S. precipitation MAE averaged over Weeks 3-4 from FREE (blue line) and from NUDGE (red line). MAE is averaged over the area shown in the map (see main text).

Next, we subdivide the forecast improvements by cluster to investigate whether there are state-dependent improvements with nudging (see **Figure A3.3** for the composite initial states of all the clusters). Cluster #4 exhibits larger improvements compared to the other seven clusters (**Figure 3.2b**), and has a significantly larger number of hindcasts with large MAE reductions compared to reductions composited over all clusters (**Figure 3.2a**). The initial states of Cluster #4 are associated with non-cold ENSO conditions and are primarily associated with MJO phases 8, 1, and 2, with the presence of an enhanced Aleutian Low (**Figure 3.3a**) and anomalous positive precipitation anomalies in the western U.S. (**Figure A3.3**).

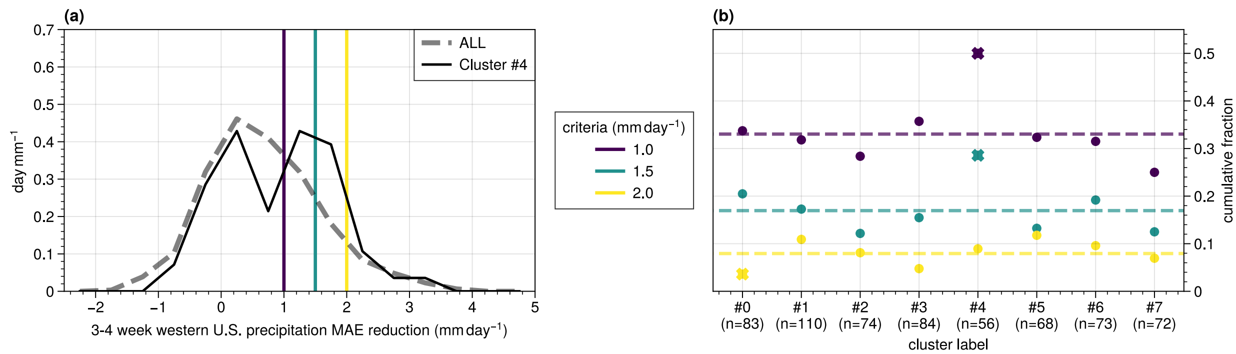

Figure 3.2. (a) The distribution of the Week 3-4 western U.S. precipitation MAE reduction associated with tropical nudging from all cases (ALL; bold gray line) and from Cluster #4 (solid black line). (b) The fraction of hindcasts having an MAE reduction greater than the thresholds as defined by the vertical lines in (a) for the ALL curve (horizontal dashed lines) and from the curve for each of the clusters (symbols). For clarity, only the distribution for Cluster #4 is shown in (a) as the solid black curve. The symbols marked as crosses are significantly different ($p < 0.05$) from the baseline fractions (horizontal dashed lines) using a two-tailed bootstrapping test with 10000 realizations.

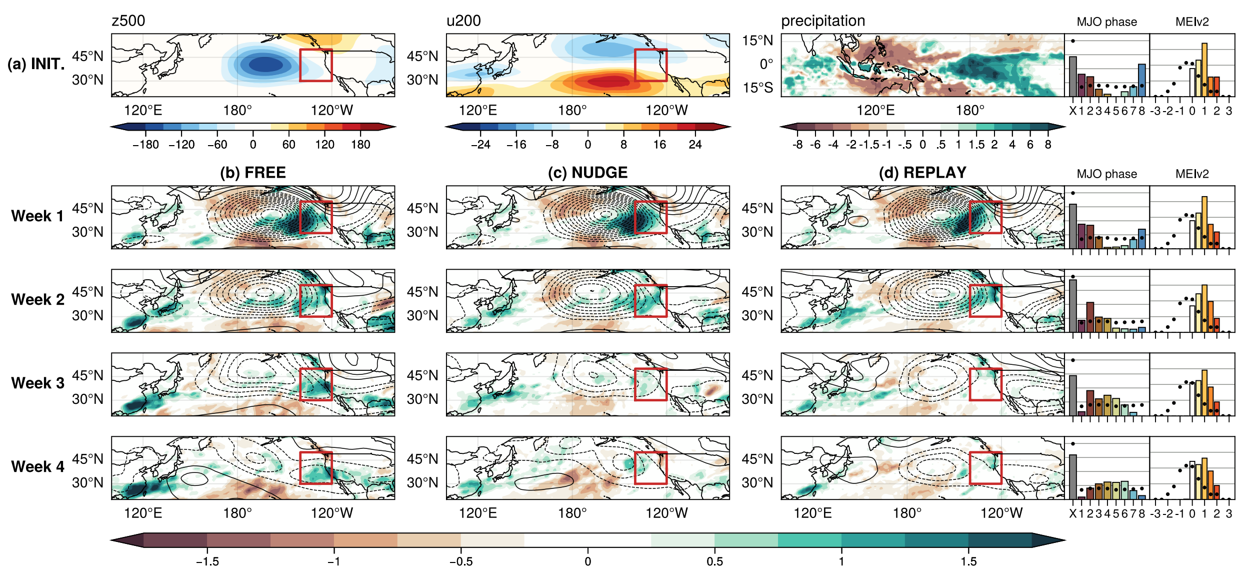

Figure 3.3. (a) the row shows the composite Day-1 states in REPLAY: z500 (left; m), u200 (middle; m s^{-1}), and precipitation (right; mm day^{-1}) anomalies from Cluster #4. The lower rows are the composites of weekly precipitation (shading; mm day^{-1}) and z500 (contours; 10-m spacing with zero omitted) anomalies for Cluster #4 in (b) FREE, (c) NUDGE, and (d) REPLAY as columns. The red box indicates where the western U.S. precipitation errors are assessed. The bar charts attached to (d) show the fraction of dates within Cluster #4 that fall in each MJO phase (non-MJO days are indicated by X) and ENSO index (MEIv2; with interval 0.5 centered at 0) for each range of lead times, where the black dots indicate the underlying fractions for all the extended boreal wintertime dates, and the gray horizontal reference lines are spaced by 10%.

To understand why Cluster #4 exhibits large improvements with nudging, it is helpful to explore how the forecast composites evolve differently in the three sets of simulations. Over the first two weeks of the forecast, FREE, NUDGE, and REPLAY all exhibit an enhanced Aleutian Low in the North Pacific and enhanced precipitation in the western U.S. (top two rows of **Figures 3.3b-d**). Over Weeks 1-2, the primary state of the MJO progresses from phases 8 to 2 in REPLAY (top two rows of **Figure 3.3d**). During Week 3, the anomalous Aleutian Low and the western U.S. precipitation are weakened in REPLAY and NUDGE (third row of **Figures 3.3c-d**). However, those weakened anomalies are not present to the same extent in the FREE simulations (third row of **Figure 3.3b**). During Week 4, anomalous 500 hPa low pressure is present over the North Pacific and the Southern U.S. but with different spatial patterns in each set of simulations. Furthermore, the western U.S. precipitation anomalies are also quite different across the three simulations in Week 4 (bottom row of **Figures 3.3b-d**), with FREE exhibiting a strong positive precipitation anomaly in the Southwest U.S. that is not present in the other two runs.

We hypothesize that the correction of intraseasonal tropical precipitation and its associated teleconnection pattern under the presence of non-cold ENSO-like states is the source of the robust forecast improvement in Week 3 for Cluster #4. In REPLAY, the initial states exhibit an enhanced Aleutian Low. This is similar to that associated with El Niño events and also is consistent with the constructive interference between non-cold ENSO and the time-lagged response to MJO phases 6-7 (Henderson and Maloney 2018). Over Weeks 1-2, similar anomalies as shown at the initial state persist with the enhanced precipitation in the western U.S. (top two rows in **Figure 3.3d**). In Week 2, a high frequency of MJO phase 2 is present (second row in **Figure 3.3d**), which is expected to excite a negative Pacific-North America (PNA) teleconnection pattern associated with positive geopotential anomalies in the Aleutian Low region in Week 3 (Tseng et al. 2019). Combined with a non-cold ENSO-like state that is associated with a positive PNA pattern and anomalous Aleutian Low, destructive interference occurs that weakens the Low as shown in (Henderson and Maloney 2018). This further decreases the western U.S. precipitation by the reduction of moisture transport associated with the anomalous Aleutian Low (Xiong et al. 2019) in REPLAY and NUDGE (third row in **Figures 3.3c-d**). However, this is much less robust in FREE (third row in **Figure 3.3b**), which we hypothesize is caused by an incorrect simulation of precipitation in the tropics and their teleconnections. **Figure 3.4a** shows that large precipitation errors exist in the deep tropics (contours) in FREE after Day 7. In particular, the model produces precipitation anomalies of excessive magnitude that resemble those anomalies associated with non-cold ENSO events, and fails to simulate the reduction after Day 7 when MJO precipitation begins to move across the Maritime Continent (shown in **Figure 3.3d** with the most frequent MJO phases transitioning from phases 8-2 in Week 1 to phases 2-4 in Week 2). Since precipitation anomalies in the deep tropics are associated with upper troposphere divergent wind anomalies that can generate stationary Rossby waves in the presence of a background vorticity gradient (Sardeshmukh and Hoskins 1988), it is likely that this precipitation error in FREE leads to failure in simulating the correct Rossby wave pattern over the North Pacific. Subsequently, it leads to incorrect simulation of the Aleutian Low and results in precipitation errors in the western U.S. that are corrected with nudging.

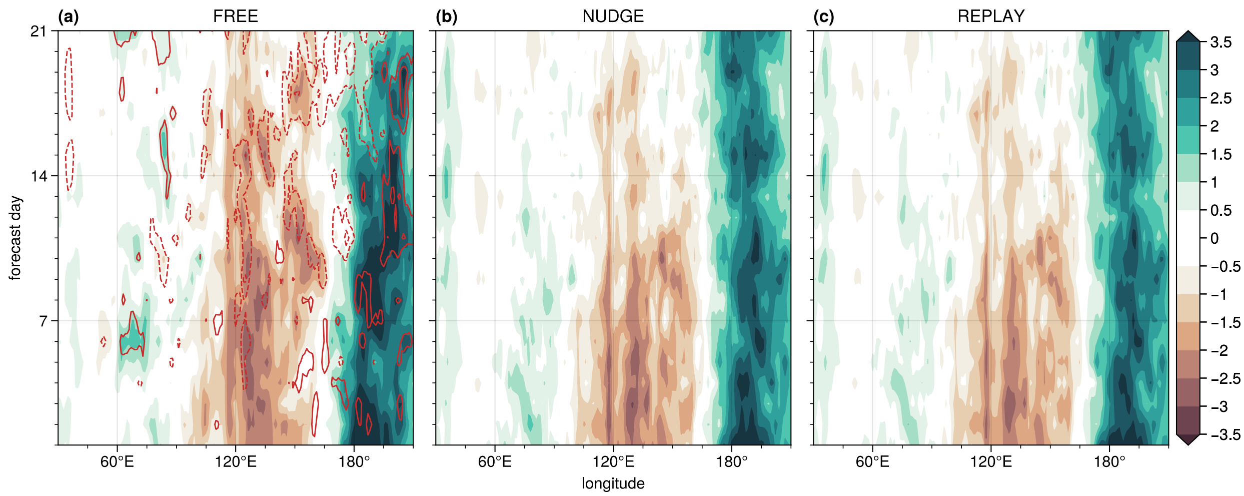

Figure 3.4. Hovmöller plots of the daily composite anomalies of 10°S-10°N precipitation (shading; mm day^{-1}) for Cluster #4 in (a) FREE, (b) NUDGE, and (c) REPLAY. The contours in (a) and (b) show the precipitation anomaly differences between the hindcasts and REPLAY with 1 mm day^{-1} spacing. The zero line is omitted.

Although the mechanism described above appears to explain Week 3, during Week 4, the states in REPLAY start to become diverse within Cluster #4 as demonstrated by an increasingly large spread in the MJO distribution in **Figure 3.3d**. Furthermore, phases 4-6 of the MJO become more common in Week 3, which were shown by (Tseng et al. 2019) to produce inconsistent teleconnections to the North Pacific. Hence, a strongly forced signal with consistent sign from the extratropics is less likely to be reflected in the composite mean, and the consistency between the composites likely no longer serves as an indicator of forecast performance. Instead, a hindcast-by-hindcast comparison is needed to evaluate the performance. Spatial correlation coefficients of Week-4 z500 anomalies over the North Pacific (20°N-70°N, 150°E-120°W) between FREE and REPLAY and between NUDGE and REPLAY are calculated to assess the midlatitude z500 forecast improvement due to tropical nudging (**Figure A3.4**). The average correlation among hindcasts is +0.17 between FREE and REPLAY and +0.41 between NUDGE and REPLAY, meaning that nudging improves the overall spatial representation of midlatitude z500 over Week

4, even though there may not be a consistently-signed signal from the tropics that forces the composite mean. However, when subsetting the hindcasts to isolate only those with the largest forecast improvements in Cluster #4, the enhanced Aleutian Low as well as the increased precipitation anomaly in the western U.S. are shown robustly to persist over Week 4 in a composite analysis in FREE but not in NUDGE and REPLAY (**Figure A3.5**), suggesting that the hypothesis of destructive interference may still be applicable to those cases in Week 4 where NUDGE performs particularly well relative to FREE.

These results strongly point to the importance of correctly representing the tropics for extratropical forecasts of precipitation three to four weeks in advance. While we have proposed a physical mechanism to explain the enhanced improvements in Cluster #4 with tropical nudging, we still have not addressed why Cluster #4 alone provides larger forecast improvements relative to other clusters. We propose some possible reasons here. First, there is greater opportunity for forecast errors and improvement when the precipitation magnitudes in REPLAY are already large. This is the case for Clusters #3, #4 and #5, as seen in **Figure A3.3**. Second, precipitation over the Indo-Pacific warm pool region (10°S-10°N, 60°E-170°E) has been shown to generate teleconnection patterns that strongly affect the weather in the western U.S. on S2S timescales (Tseng et al. 2019), with MJO phases 2 and 3 providing particularly strong forcing 7-10 days later. In Weeks 1-2 during MJO phases 2-4, this region is poorly represented in FREE but is improved more after the nudging (**Figure A3.6**). Only the MJO in Cluster #2 and Cluster #4 in Weeks 1-2 has higher frequencies in phases 2-4 (**Figure A3.7**). Third, the background states of different clusters provide different waveguide properties for stationary Rossby waves. Thus, it is possible that the western U.S. is less modulated by the teleconnection in other clusters compared to Cluster #4, while other locations might show a stronger modulation.

The multivariate k-means clustering method is capable of capturing features in the initial states important for the forecast improvement, which includes a strong anomalous Aleutian Low. Conditioning the forecasts on ENSO index and MJO phase (e.g. MEIv2 ≥ 0 and MJO phases 1, 4, and 8; **Figure A3.8**), rather than using k-means clustering, also yields statistically significant forecast improvement, however. This is perhaps not surprising, as it is well known that ENSO and MJO teleconnections can also modulate the Aleutian Low (e.g. Henderson and Maloney 2018). Even so, the composites of all hindcasts with non-cold ENSO that are initially in MJO phases 8 and 1 do not show an enhanced Aleutian Low as strong as in Cluster #4 (**Figure A3.9**). This is possibly because not all MJO and ENSO events in these phases strongly modulate the Aleutian Low. For example, the strength of the MJO teleconnection to the extratropics is also modulated by other factors such as the strength of the tropical quasi-biennial oscillation (Toms et al. 2020). The k-means clustering approach thus allows us to focus on initial states that feature an enhanced anomalous Aleutian Low, whether or not those days map onto specific climate indices (see the relatively wide spread of MJO and ENSO indices in the bar chart of **Figure 3.3a**). We leverage the advantage of clustering that it provides and propose an underlying mechanism that would have been more difficult to isolate using MJO and ENSO metrics alone.

3.4 Summary

Extended-range precipitation forecast improvements along the U.S. West Coast in NOAA/NCEP GFS v15.1.1 are examined in hindcasts where tropical fields of horizontal wind, mass, temperature, and humidity are nudged toward observations. With nudging, the forecast mean absolute error of the western U.S. precipitation is reduced over Weeks 3-4 (**Figure 3.1** and **Figure**

A3.1), with larger reductions during forecast periods that were particularly poorly simulated in the FREE (i.e. un-nudged) simulations (**Figure A3.2**), consistent with the findings in Dias et al. (2021).

A conditional forecast improvement analysis is performed based on a multivariate clustering method. One specific cluster (Cluster #4), characterized by initial states with a strong Aleutian Low and weighted toward non-cold ENSO conditions and MJO phases 8-2 (**Figure 3.3a**), is shown to provide significantly larger forecast improvements in western U.S. precipitation (**Figure 3.2**). The robust improvements can be explained by an interaction that is not simulated well in the free running simulations (FREE), but is well-represented in the nudged simulations (NUDGE): a strong Aleutian Low is subsequently weakened after two weeks by the destructive interference associated with the MJO phases 8-2 teleconnection pattern (**Figures 3.3b-d**) under non-cold ENSO conditions. The poor representation of tropical intraseasonal precipitation variability in the FREE simulations (**Figure 3.4a**) is suggested to produce an unrealistic interaction between the Aleutian Low and the MJO teleconnection pattern, leading to errors in the z500 and precipitation pattern near the western U.S. These errors are corrected in the nudged simulations (**Figures 3.3b-d** and **Figure 3.4b**).

We did not perform an exhaustive evaluation of the model improvements for every cluster, choosing instead to concentrate on Cluster #4 since it exhibits substantially greater improvements for the western U.S. precipitation in Weeks 3-4. It is possible that other clusters provide better forecast improvements with nudging at other locations, which could be examined in a future study. More sets of tropical nudging experiments, including those with nudging only being applied for a narrower latitudinal band, and over shorter time periods including over only the first week or two of the hindcasts, were also conducted by Dias et al. (2021). These experiments might also be useful for examining some of the proposed mechanisms above.

Note that the clustering method provides an alternative to using conventional ENSO and MJO metrics to analyze conditional forecast improvement. The clustering method shows that forecast improvements for the western U.S. precipitation are largest when an anomalously strong Aleutian Low is present in the initial condition, which subsequently gets perturbed by the evolution of the tropics. A major implication of this study is that improving forecasts of intraseasonal precipitation evolution in the tropics, especially that during MJO phases 8 and 1-4 under non-cold ENSO states, might be a key to producing better S2S precipitation forecasts in the western U.S.

CHAPTER 4

Summary

In this thesis, we try to answer two questions that are crucial for understanding and improving S2S weather forecast skill: (1) How and why has the MJO evolved with climate warming over the observational record? (2) What initial states are associated with forecast errors on S2S timescales in an operational weather model? These two questions have been addressed in this thesis in Chapter 2 and Chapter 3, and our findings are summarized below in Subsections 4.1 and 4.2.

4.1 Recent changes in the MJO and their underlying mechanisms

In recent work analyzing climate projections under a warming scenario, a decrease in the ratio of MJO circulation to precipitation anomaly amplitude is found to be detectable as early as 2021–2040 (Bui and Maloney 2019), consistent with an increase in dry static stability as predicted by tropical weak temperature gradient balance (Knutson and Manabe 1995). In Chapter 2, we examined MJO activity in multiple reanalyses (ERA5, MERRA-2, and ERA-20C) and find that while MJO wind and precipitation anomaly amplitudes have a complicated time evolution over the observational record, a decrease in the ratio of MJO circulation to precipitation anomaly amplitude is detectable over the observational period. This change is consistent with that theoretically predicted given the increase in tropical dry static stability that has occurred with climate warming. These results suggest that weak temperature gradient theory may be able to help explain changes in MJO activity in recent decades. Since the upper-tropospheric MJO divergence is weakened per unit MJO precipitation, the efficiency with which MJO precipitation can excite stationary Rossby wave trains over the extratropics may have also decreased with climate warming, although this interpretation is complicated by potential changes in the basic state vorticity gradients that were not examined. Our analysis suggests that the sources of S2S predictability from the MJO might be modified in a warming climate.

4.2 State-dependent S2S forecast skill over the western United States

In Chapter 3, boreal-wintertime hindcasts in the Unified Forecast System with the tropics nudged toward reanalysis is found to improve western United States precipitation forecasts at 3-4 week lead times when compared to those without nudging. To diagnose the origin of these improvements, a multivariate k-means clustering method is used to group hindcasts into subsets by their initial conditions. One cluster characterized by an initially strong Aleutian Low demonstrates larger improvements at 3-4 weeks compared to other clusters. The greater improvement with nudging for this cluster originates from the incorrect simulation of destructive interference between (1) the anomalous Aleutian Low and (2) the teleconnection pattern excited by certain phases of the MJO during non-cold ENSO conditions in the non-nudged hindcasts. The results suggest that improving forecasts of tropical intraseasonal precipitation, especially that during the early MJO phases under non-cold ENSO, might be important in producing better 3-4 week precipitation forecasts in the western United States.

4.3 Future Perspectives

To better characterize recent changes to the MJO with climate warming, further work using observational data with longer time spans and from different models and instruments would be useful to validate the findings in Chapter 2. For example, in situ and satellite observations could provide more accurate precipitation estimates since the precipitation used in this thesis is calculated by parameterization methods in the reanalyses. Wind data from radiosonde that covers the time back to the beginning of the 20th century could also be used to validate our findings (e.g. Durre et al. 2018).

As described in Subsection 3.4, more sets of tropical nudging experiments, including those with nudging only being applied for a narrower latitudinal band, and over shorter time periods (e.g. the first week or two of the hindcasts), were also conducted by Dias et al. (2021). Those experiments could be analyzed to further validate the mechanism of destructive interference of the anomalous Aleutian Low. For example, we expect similar 3-4 week forecasts improvements to be presented in Cluster #4 in the experiment with only the first two week being nudged in the tropics, since we hypothesized that the improvement originates from the corrected simulation in the tropics over the second week.

In Chapter 3, a multivariate k-means clustering method is used to identify conditional forecast improvement with few *a priori* assumptions being imposed. The findings suggest the great potential of unsupervised machine learning techniques in the field of atmospheric science. Those methods provide a way to reveal unrecognized properties of certain climate states that are important for the quantities of interest (e.g. forecast skill).

Based on the changing nature of the MJO over the last century found in Chapter 2, the physical pathway that leads to the state-dependent improvements due to the nudging identified in Chapter 3 may be modified with a warming climate. To investigate such a potential modification on the teleconnection, not only the change in the MJO but also the evolution of the basic state under the warming climate are needed to be examined. For example, the change in background subtropical jets could lead to different RWS patterns at certain MJO phases and different paths of which the stationary Rossby waves propagate (e.g. Bui 2020).

REFERENCES

Allen, R. J., and S. C. Sherwood, 2008: Warming maximum in the tropical upper troposphere deduced from thermal winds. *Nat. Geosci.*, **1**, 399–403, https://doi.org/10.1038/ngeo208.

Arnold, N. P., Z. Kuang, and E. Tziperman, 2013: Enhanced MJO-like Variability at High SST. *J. Clim.*, **26**, 988–1001, https://doi.org/10.1175/JCLI-D-12-00272.1.

Bauer, P., A. Thorpe, and G. Brunet, 2015: The quiet revolution of numerical weather prediction. *Nature*, **525**, 47–55, https://doi.org/10.1038/nature14956.

Bielli, S., H. Douville, and B. Pohl, 2010: Understanding the West African monsoon variability and its remote effects: an illustration of the grid point nudging methodology. *Clim. Dyn.*, **35**, 159–174, https://doi.org/10.1007/s00382-009-0667-8.

Bloom, S. C., L. L. Takacs, A. M. da Silva, and D. Ledvina, 1996: Data Assimilation Using Incremental Analysis Updates. *Mon. Weather Rev.*, **124**, 1256–1271, https://doi.org/10.1175/1520-0493(1996)124<1256:DAUIAU>2.0.CO;2.

Branstator, G., 2014: Long-Lived Response of the Midlatitude Circulation and Storm Tracks to Pulses of Tropical Heating. *J. Clim.*, **27**, 8809–8826, https://doi.org/10.1175/JCLI-D-14-00312.1.

Bui, H. X., 2020: Increased impacts on US West Coast. *Nat. Clim. Chang.*, **10**, 603–604, https://doi.org/10.1038/s41558-020-0828-7.

——, and E. D. Maloney, 2018: Changes in Madden-Julian Oscillation Precipitation and Wind Variance Under Global Warming. *Geophys. Res. Lett.*, **45**, 7148–7155.

——, and ——, 2019: Transient Response of MJO Precipitation and Circulation to Greenhouse Gas Forcing. *Geophys. Res. Lett.*, **46**, 13546–13555, https://doi.org/10.1029/2019GL085328.

Chen, M., W. Wang, and A. Kumar, 2010: Prediction of Monthly-Mean Temperature: The Roles of Atmospheric and Land Initial Conditions and Sea Surface Temperature. *J. Clim.*, **23**, 717–725, https://doi.org/10.1175/2009JCLI3090.1.

Chikira, M., 2014: Eastward-Propagating Intraseasonal Oscillation Represented by Chikira–Sugiyama Cumulus Parameterization. Part II: Understanding Moisture Variation under Weak Temperature Gradient Balance. *J. Atmos. Sci.*, **71**, 615–639, https://doi.org/10.1175/JAS-D-13-038.1.

Dee, D. P., and Coauthors, 2011: The ERA-Interim reanalysis: configuration and performance of the data assimilation system. *Quart. J. Roy. Meteor. Soc.*, **137**, 553–597, https://doi.org/10.1002/qj.828.

Dias, J., S. N. Tulich, M. Gehne, and G. N. Kiladis, 2021: Tropical origins of Weeks 2-4 forecasts errors during Northern Hemisphere cool season. *Mon. Weather Rev.*, **1**, https://doi.org/10.1175/MWR-D-21-0020.1.

Doblas-Reyes, F. J., J. García-Serrano, F. Lienert, A. P. Biescas, and L. R. L. Rodrigues, 2013: Seasonal climate predictability and forecasting: status and prospects. *Wiley Interdiscip. Rev. Clim. Change*, **4**, 245–268, https://doi.org/10.1002/wcc.217.

Durre, I., X. Yin, R. S. Vose, S. Applequist, and J. Arnfield, 2018: Enhancing the Data Coverage in the Integrated Global Radiosonde Archive. *J. Atmos. Ocean. Technol.*, **35**, 1753–1770, https://doi.org/10.1175/JTECH-D-17-0223.1.

Ferranti, L., T. N. Palmer, F. Molteni, and E. Klinker, 1990: Tropical-Extratropical Interaction Associated with the 30–60 Day Oscillation and Its Impact on Medium and Extended Range Prediction. *J. Atmos. Sci.*, **47**, 2177–2199, https://doi.org/10.1175/1520-0469(1990)047<2177:TEIAWT>2.0.CO;2.

Gelaro, R., and Coauthors, 2017: The Modern-Era Retrospective Analysis for Research and Applications, Version 2 (MERRA-2). *J. Clim.*, **30**, 5419–5454, https://doi.org/10.1175/JCLI-D-16-0758.1.

Henderson, S. A., and E. D. Maloney, 2018: The Impact of the Madden–Julian Oscillation on High-Latitude Winter Blocking during El Niño–Southern Oscillation Events. *J. Clim.*, **31**, 5293–5318, https://doi.org/10.1175/JCLI-D-17-0721.1.

Hendon, H. H., B. Liebmann, M. Newman, J. D. Glick, and J. E. Schemm, 2000: Medium-Range Forecast Errors Associated with Active Episodes of theMadden–Julian Oscillation. *Mon. Weather Rev.*, **128**, 69–86, https://doi.org/10.1175/1520-0493(2000)128<0069:MRFEAW>2.0.CO;2.

Henley, B. J., J. Gergis, D. J. Karoly, S. Power, J. Kennedy, and C. K. Folland, 2015: A Tripole Index for the Interdecadal Pacific Oscillation. *Clim. Dyn.*, **45**, 3077–3090, https://doi.org/10.1007/s00382-015-2525-1.

Hersbach, H., and Coauthors, 2020: The ERA5 global reanalysis. *Q.J.R. Meteorol. Soc.*, **64**, 29, https://doi.org/10.1002/qj.3803.

Holloway, C. E., and J. D. Neelin, 2009: Moisture Vertical Structure, Column Water Vapor, and Tropical Deep Convection. *J. Atmos. Sci.*, **66**, 1665–1683, https://doi.org/10.1175/2008JAS2806.1.

Hoskins, B. J., and D. J. Karoly, 1981: The steady linear response of a spherical atmosphere to thermal and orographic forcing. *J. Atmos. Sci.*, **38**, 1179–1196, https://doi.org/10.1175/1520-0469(1981)038<1179:tslroa>2.0.co;2.

——, and T. Ambrizzi, 1993: Rossby Wave Propagation on a Realistic Longitudinally Varying Flow. *J. Atmos. Sci.*, **50**, 1661–1671, https://doi.org/10.1175/1520-0469(1993)050<1661:RWPOAR>2.0.CO;2.

Hudson, D., O. Alves, H. H. Hendon, and A. G. Marshall, 2011: Bridging the gap between weather and seasonal forecasting: intraseasonal forecasting for Australia. *Quart. J. Roy. Meteor. Soc.*, **137**, 673–689, https://doi.org/10.1002/qj.769.

Jones, C., and L. M. V. Carvalho, 2006: Changes in the Activity of the Madden–Julian Oscillation during 1958–2004. *J. Clim.*, **19**, 6353–6370, https://doi.org/10.1175/JCLI3972.1.

Jung, T., M. J. Miller, and T. N. Palmer, 2010: Diagnosing the Origin of Extended-Range Forecast Errors. *Mon. Weather Rev.*, **138**, 2434–2446, https://doi.org/10.1175/2010MWR3255.1.

Kiladis, G. N., K. H. Straub, and P. T. Haertel, 2005: Zonal and Vertical Structure of the Madden–Julian Oscillation. *J. Atmos. Sci.*, **62**, 2790–2809, https://doi.org/10.1175/JAS3520.1.

——, J. Dias, K. H. Straub, M. C. Wheeler, S. N. Tulich, K. Kikuchi, K. M. Weickmann, and M. J. Ventrice, 2014: A Comparison of OLR and Circulation-Based Indices for Tracking the MJO. *Mon. Weather Rev.*, **142**, 1697–1715, https://doi.org/10.1175/mwr-d-13-00301.1.

Knutson, T. R., and S. Manabe, 1995: Time-Mean Response over the Tropical Pacific to Increased C02 in a Coupled Ocean-Atmosphere Model. *J. Clim.*, **8**, 2181–2199, https://doi.org/10.1175/1520-0442(1995)008<2181:TMROTT>2.0.CO;2.

Lloyd, S. P., 1982: Least squares quantization in pcm. *IEEE Transactions on Information Theory* https://citeseerx.ist.psu.edu/viewdoc/summary?doi=10.1.1.131.1338 (Accessed July 2, 2021).

Lorenz, E. N., 1956: *Empirical orthogonal functions and statistical weather prediction*. Massachusetts Institute of Technology, Department of Meteorology,.

Madden, R. A., and P. R. Julian, 1971: Detection of a 40–50 Day Oscillation in the Zonal Wind in the Tropical Pacific. *J. Atmos. Sci.*, **28**, 702–708, https://doi.org/10.1175/1520-0469(1971)028<0702:DOADOI>2.0.CO;2.

——, and ——, 1972: Description of global-scale circulation cells in the tropics with a 40--50 day period. *J. Atmos. Sci.*, **29**, 1109–1123, https://doi.org/10.1175/1520-0469(1972)029<1109:DOGSCC>2.0.CO;2.

Maloney, E. D., and S.-P. Xie, 2013: Sensitivity of tropical intraseasonal variability to the pattern of climate warming: MJO ACTIVITY AND CLIMATE WARMING. *J. Adv. Model. Earth Syst.*, **5**, 32–47, https://doi.org/10.1029/2012MS000171.

——, Á. F. Adames, and H. X. Bui, 2019: Madden–Julian oscillation changes under anthropogenic warming. *Nat. Clim. Chang.*, **9**, 26–33, https://doi.org/10.1038/s41558-018-0331-6.

Mantua, N. J., S. R. Hare, Y. Zhang, J. M. Wallace, and R. C. Francis, 1997: A Pacific Interdecadal Climate Oscillation with Impacts on Salmon Production*. *Bull. Am. Meteorol. Soc.*, **78**, 1069–1080, https://doi.org/10.1175/1520-0477(1997)078<1069:APICOW>2.0.CO;2.

Matthews, A. J., B. J. Hoskins, and M. Masutani, 2004: The global response to tropical heating in the Madden–Julian oscillation during the northern winter. *Quart. J. Roy. Meteor. Soc.*, **130**, 1991–2011, https://doi.org/10.1256/qj.02.123.

National Centers for Environmental Information, U.S. Billion-dollar Weather and Climate Disasters, 1980 - present (NCEI Accession 0209268). https://doi.org/10.25921/stkw-7w73.

Oliver, E. C. J., and K. R. Thompson, 2012: A Reconstruction of Madden–Julian Oscillation Variability from 1905 to 2008. *J. Clim.*, **25**, 1996–2019, https://doi.org/10.1175/JCLI-D-11-00154.1.

Pedregosa, F., and Coauthors, 2011: Scikit-learn: Machine Learning in Python. *J. Mach. Learn. Res.*, **12**, 2825–2830.

Poli, P., and Coauthors, 2016: ERA-20C: An Atmospheric Reanalysis of the Twentieth Century. *J. Clim.*, **29**, 4083–4097, https://doi.org/10.1175/JCLI-D-15-0556.1.

Robertson, A. W., A. Kumar, M. Peña, and F. Vitart, 2015: Improving and Promoting Subseasonal to Seasonal Prediction. *Bull. Am. Meteorol. Soc.*, **96**, ES49–ES53, https://doi.org/10.1175/BAMS-D-14-00139.1.

Sardeshmukh, P. D., and B. J. Hoskins, 1988: The Generation of Global Rotational Flow by Steady Idealized Tropical Divergence. *J. Atmos. Sci.*, **45**, 1228–1251, https://doi.org/10.1175/1520-0469(1988)045<1228:TGOGRF>2.0.CO;2.

Sherwood, S. C., and N. Nishant, 2015: Atmospheric changes through 2012 as shown by iteratively homogenized radiosonde temperature and wind data (IUKv2). *Environ. Res. Lett.*, **10**, 054007, https://doi.org/10.1088/1748-9326/10/5/054007.

Slingo, J. M., D. P. Rowell, K. R. Sperber, and F. Nortley, 1999: On the predictability of the interannual behaviour of the Madden-Julian Oscillation and its relationship with El Niño. *Quart. J. Roy. Meteor. Soc.*, **125**, 583–609, https://doi.org/10.1002/qj.49712555411.

Sobel, A. H., and C. S. Bretherton, 2000: Modeling Tropical Precipitation in a Single Column. *J. Clim.*, **13**, 4378–4392, https://doi.org/10.1175/1520-0442(2000)013<4378:MTPIAS>2.0.CO;2.

Tao, L., J. Zhao, and T. Li, 2015: Trend analysis of tropical intraseasonal oscillations in the summer and winter during 1982-2009: TREND ANALYSIS OF BSISO AND MJO DURING 1982-2009. *Int. J. Climatol.*, **35**, 3969–3978, https://doi.org/10.1002/joc.4258.

Toms, B. A., E. A. Barnes, E. D. Maloney, and S. C. Heever, 2020: The global teleconnection signature of the madden-Julian oscillation and its modulation by the quasi-biennial oscillation. *J. Geophys. Res.*, **125**, https://doi.org/10.1029/2020jd032653.

Trenberth, K. E., and D. P. Stepaniak, 2001: Indices of El Niño Evolution. *J. Clim.*, **14**, 1697–1701, https://doi.org/10.1175/1520-0442(2001)014<1697:LIOENO>2.0.CO;2.

Tseng, K.-C., E. Maloney, and E. Barnes, 2019: The Consistency of MJO Teleconnection Patterns: An Explanation Using Linear Rossby Wave Theory. *J. Clim.*, **32**, 531–548, https://doi.org/10.1175/JCLI-D-18-0211.1.

Vitart, F., and F. Molteni, 2010: Simulation of the Madden- Julian Oscillation and its teleconnections in the ECMWF forecast system. *Quart. J. Roy. Meteor. Soc.*, **136**, 842–855, https://doi.org/10.1002/qj.623.

——, A. W. Robertson, and D. L. T. Anderson, 2012: Subseasonal to Seasonal Prediction Project: Bridging the gap between weather and climate. *Bulletin of the World Meteorological Organization*, **61**, 23.

White, C. J., and Coauthors, 2017: Potential applications of subseasonal-to-seasonal (S2S) predictions. *Meteorol. Appl.*, **24**, 315–325, https://doi.org/10.1002/met.1654.

Wolding, B. O., and E. D. Maloney, 2015: Objective Diagnostics and the Madden–Julian Oscillation. Part II: Application to Moist Static Energy and Moisture Budgets. *J. Clim.*, **28**, 7786–7808, https://doi.org/10.1175/JCLI-D-14-00689.1.

——, ——, and M. Branson, 2016: Vertically resolved weak temperature gradient analysis of the Madden-Julian Oscillation in SP-CESM: WTG ANALYSIS OF THE MJO IN SP-CESM. *J. Adv. Model. Earth Syst.*, **8**, 1586–1619, https://doi.org/10.1002/2016MS000724.

Xiong, Y., Q. Chen, and X. Ren, 2019: Influence of Boreal Winter Intraseasonal Variation of Aleutian Low on Water Vapor Transport and Atmospheric Rivers. *Atmosphere* , **10**, 49, https://doi.org/10.3390/atmos10020049.

Yanai, M., S. Esbensen, and J.-H. Chu, 1973: Determination of Bulk Properties of Tropical Cloud Clusters from Large-Scale Heat and Moisture Budgets. *J. Atmos. Sci.*, **30**, 611–627, https://doi.org/10.1175/1520-0469(1973)030<0611:DOBPOT>2.0.CO;2.

Yin, X., A. Gruber, and P. Arkin, 2004: Comparison of the GPCP and CMAP Merged Gauge–Satellite Monthly Precipitation Products for the Period 1979–2001. *J. Hydrometeorol.*, **5**, 1207–1222, https://doi.org/10.1175/JHM-392.1.

Zhang, C., 2013: Madden–Julian Oscillation: Bridging Weather and Climate. *Bull. Am. Meteorol. Soc.*, **94**, 1849–1870, https://doi.org/10.1175/BAMS-D-12-00026.1.

Zhang, T., A. Hoell, J. Perlwitz, J. Eischeid, D. Murray, M. Hoerling, and T. M. Hamill, 2019: Towards probabilistic multivariate ENSO monitoring. *Geophys. Res. Lett.*, **46**, 10532–10540, https://doi.org/10.1029/2019gl083946.

APPENDIX A

Model and Experimental Setup Used in Chapter 3

In this study, we utilize the nudging simulations of Dias et al. (2021) conducted using a leading U.S. forecast model. Specifically, version 15.1.1 of the NOAA/ National Centers for Environmental Prediction Global Forecast System (NOAA/NCEP GFS v15.1.1) is used with C128 horizontal resolution and 64 vertical levels from the surface to 1 hPa. Other operational settings such as the lower boundary condition and physical parameterizations used are provided in detail here: https://www.emc.ncep.noaa.gov/emc/pages/numerical_forecast_systems/gfs/implementations.php. As described in more detail below, three sets of simulations are conducted: ***REPLAY***, where the whole globe is nudged toward the observed state represented by ERA-Interim reanalysis (Dee et al. 2011) at all lead times; ***FREE***, where the model freely evolves after initialization to produce forecasts (one can think of this as the default forecast behavior), and ***NUDGE***, where only the tropics are nudged at all lead times toward the reanalysis. Differences in forecast errors between FREE and NUDGE relative to REPLAY thus indicate how representation of the tropics can affect forecast performance.

The incremental analysis update (IAU; Bloom et al. 1996) scheme is utilized to nudge the model toward the observed state to create the REPLAY simulation. Briefly, the IAU is implemented with 6-hour cycles using the following procedure: the differences in the observations and the forecasted fields are computed at the end of a 3-hour free forecast as a forcing tendency, and the forecast is run again for 6 hours with the forcing applied (see Figure 1 in Dias et al. 2021). The fields of zonal and meridional winds, mass, temperature, and specific humidity are nudged.

When the whole globe is nudged, a good approximation of the observed state is produced, here referred to as REPLAY.

A second set of hindcasts, FREE, are performed to evaluate the forecast performance of the model in free-running mode (i.e. with no nudging). In this setting, the model is run freely out to 30 days from the restart points provided by REPLAY. A third set of hindcasts, NUDGE, are performed to assess the effect on S2S forecast performance in the extratropics when the tropics are represented accurately. The design of NUDGE is the same as FREE, except that the nudging method used in REPLAY is applied within 30°S-30°N using a weighting function that is unity between 10°S-10°N and is reduced to zero toward 30°N and 30°S following a hyperbolic tangent curve. Note that the same form of tropical nudging was used in Jung et al. (2010) and Dias et al. (2021).

All three sets of simulations are run during November 1999 to April 2018 for the extended boreal winter (November to April). At the beginning of each season, the model is initialized with the ensemble mean fields from Global Ensemble Forecast System version 12 (GEFSv12) on November 1st. The hindcast runs (FREE and NUDGE) are initialized every 5 days afterward using the restart files output from REPLAY until the end of March in the following year. Thus, 31 hindcasts are performed for each extended boreal winter with 620 hindcasts in total. The 3-hourly output from the model is regridded to 1° by 1° horizontal grid spacing and averaged to daily means prior to the subsequent analysis.

APPENDIX B

Supplementary Figures

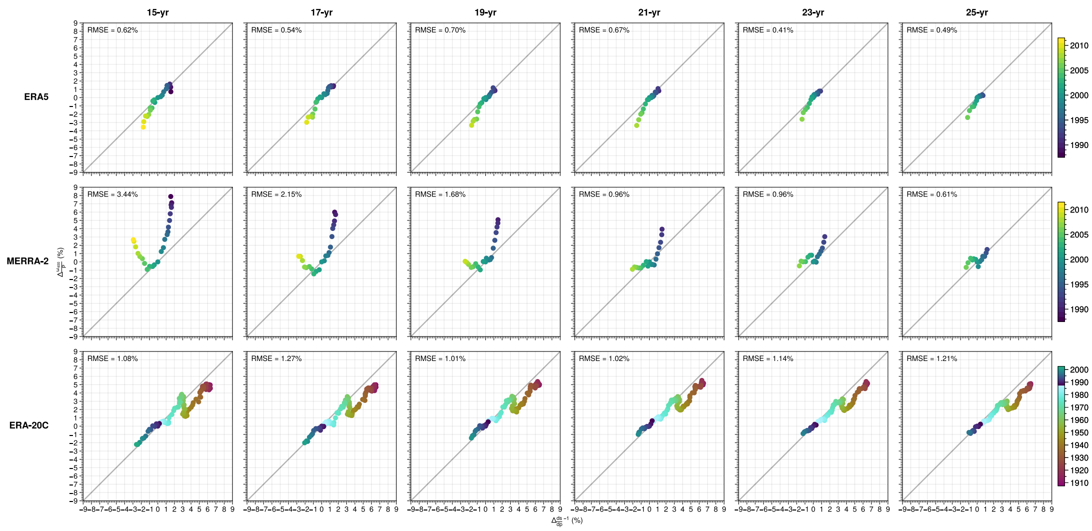

Figure A2.1. As **Figure 2.3**, but using 15, 17, 19, 21, 23, and 25-year running composites. Note that the reference years used in ERA5, MERRA-2, and ERA-20C are 2000, 2000, and 1990 as central years to make the colors consistent among different lengths of running windows.

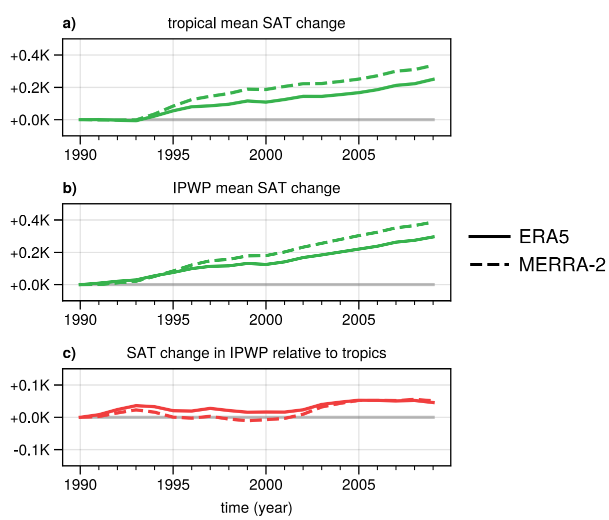

Figure A2.2. The boreal-wintertime changes of the 19-years running means of (a) surface air temperature within the tropics (15∘S-15∘N), (b) surface air temperature in the IPWP region, and (c) the change in the IPWP region relative to the tropics, equivalent to (b) minus (a). Solid lines are from ERA5 and dashed lines are from MERRA-2.

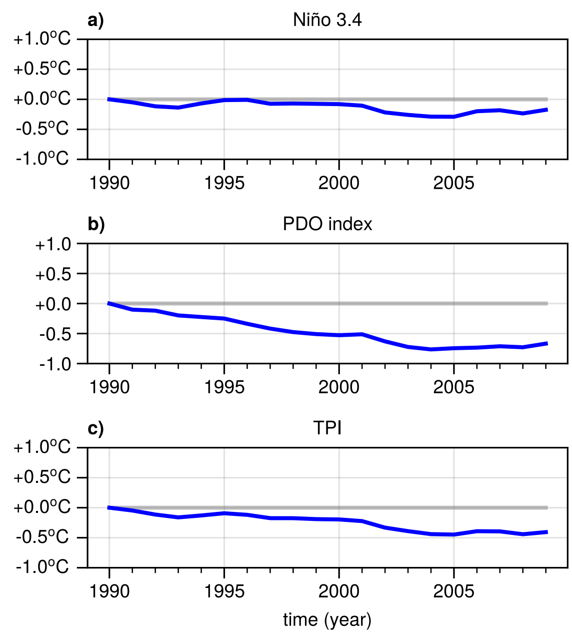

Figure A2.3. The boreal-wintertime changes of the 19-years running means of (a) the Niño 3.4 SST (Trenberth and Stepaniak 2001), (b) the unfiltered Pacific Decadal Oscillation (PDO) index (Mantua et al. 1997), and (c) the unfiltered Interdecadal-Pacific-Oscillation (IPO) tripole SST index (TPI; Henley et al. 2015).

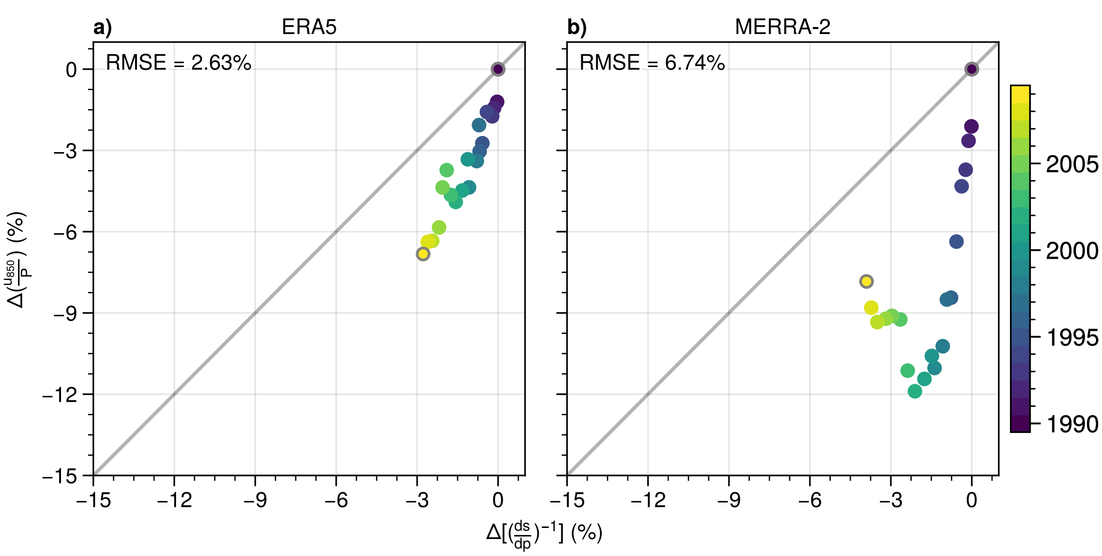

Figure A2.4. As **Figure 2.3a-b**, but the *y*-axis is the ratio of MJO u_{850} to precipitation amplitude.

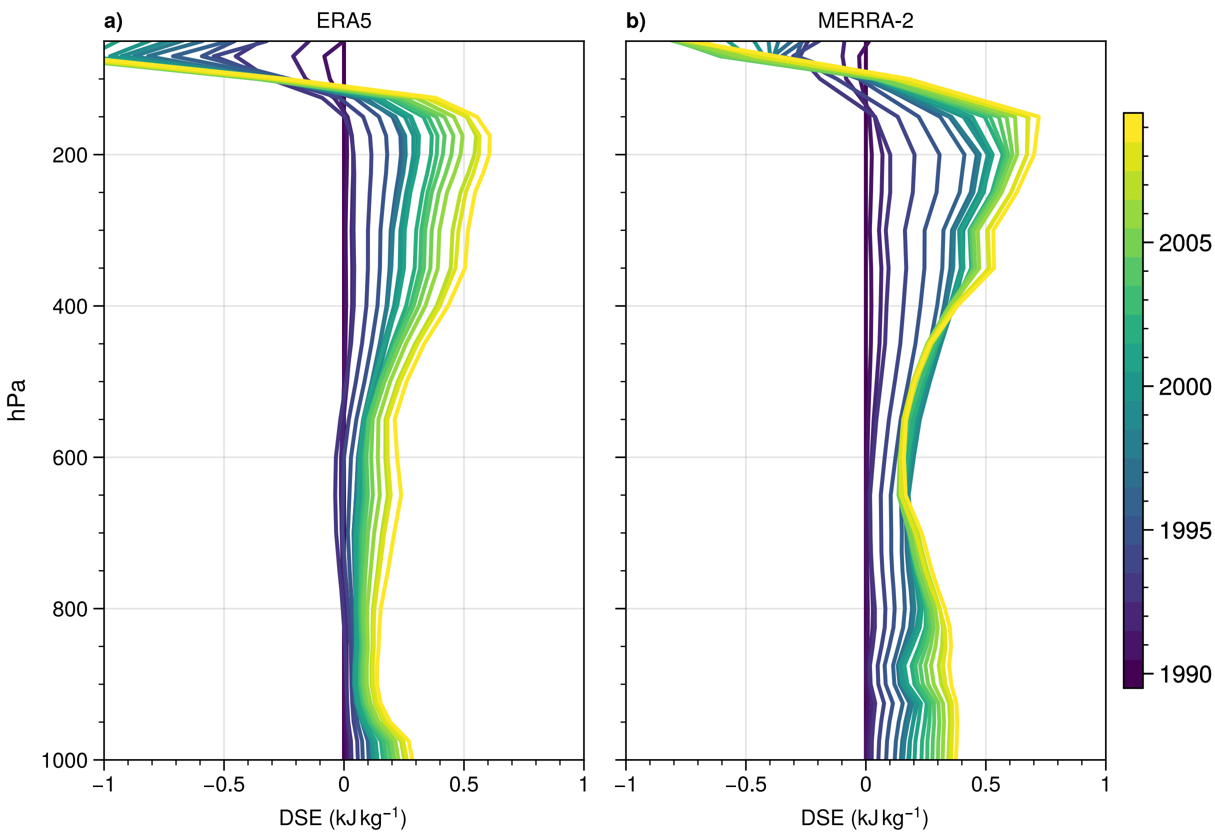

Figure A2.5. The changes of boreal-wintertime composite DSE between the 19-years running windows and the early period in ERA5 and MERRA-2. The color indicates the central year of the running windows.

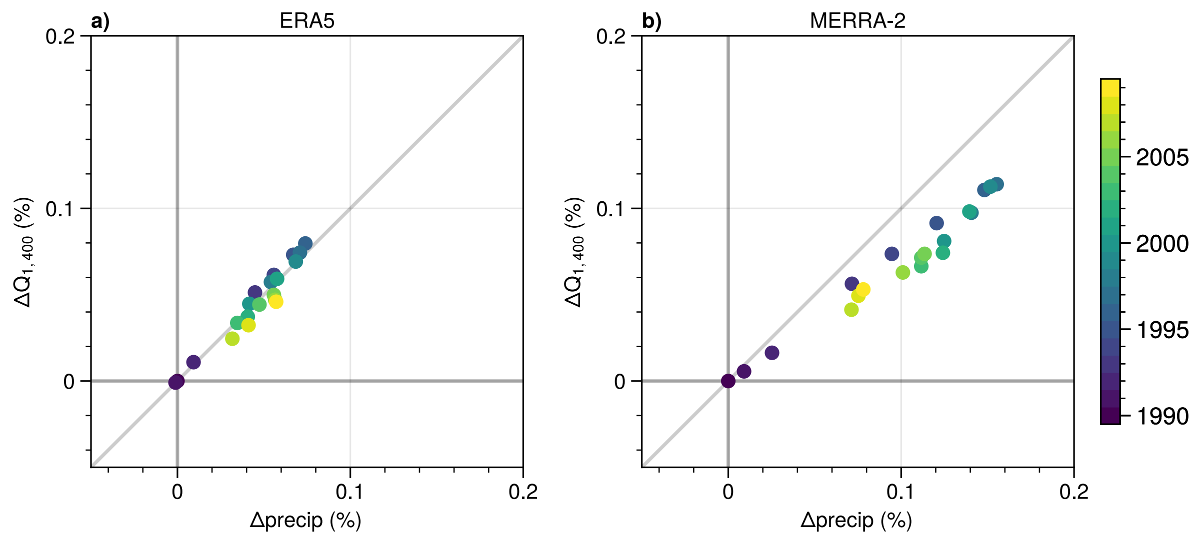

Figure A2.6. As **Figure 2.3a-b**, but the relative change in boreal-wintertime MJO anomaly amplitudes of (*x*-axis) precipitation and (*y*-axis) apparent heat source at 400 hPa ($Q_{1,400}$). The grey diagonal line is one-to-one, indicating that MJO precipitation has the same percentage change as MJO $Q_{1,400}$. $Q_{1,400}$ was derived as a residual in the thermodynamic energy budget.

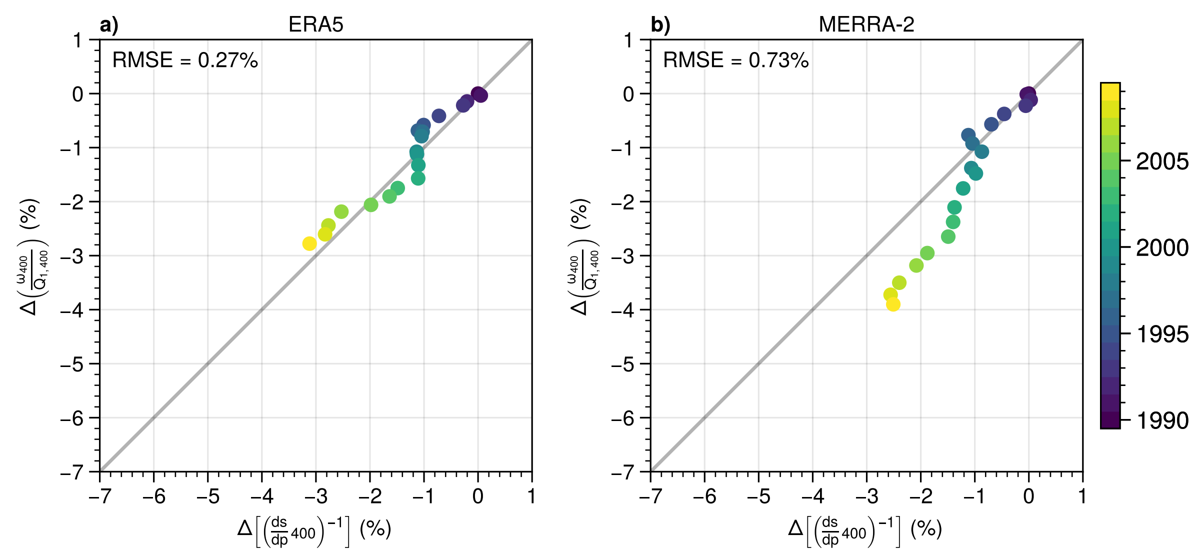

Figure A2.7. As **Figure 2.3a-b**, but shows the relative change in MJO $\omega_{400}/Q_{1,400}$ instead of MJO ω_{400}/P on the *y*-axis.

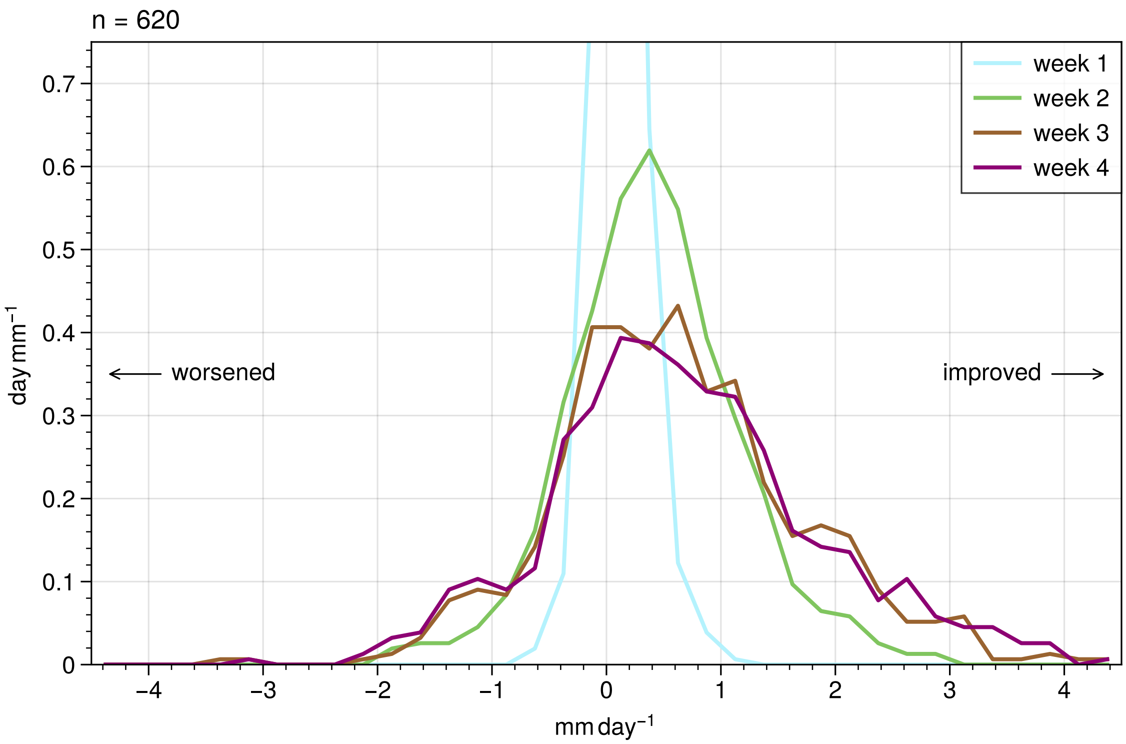

Figure A3.1. The weekly-averaged MAE reduction in the western U.S. precipitation comparing NUDGE to FREE. The Week-1 line is not fully shown as it has a high peak near zero. Notice the heavy tails of Week-3 and Week-4 lines on the right.

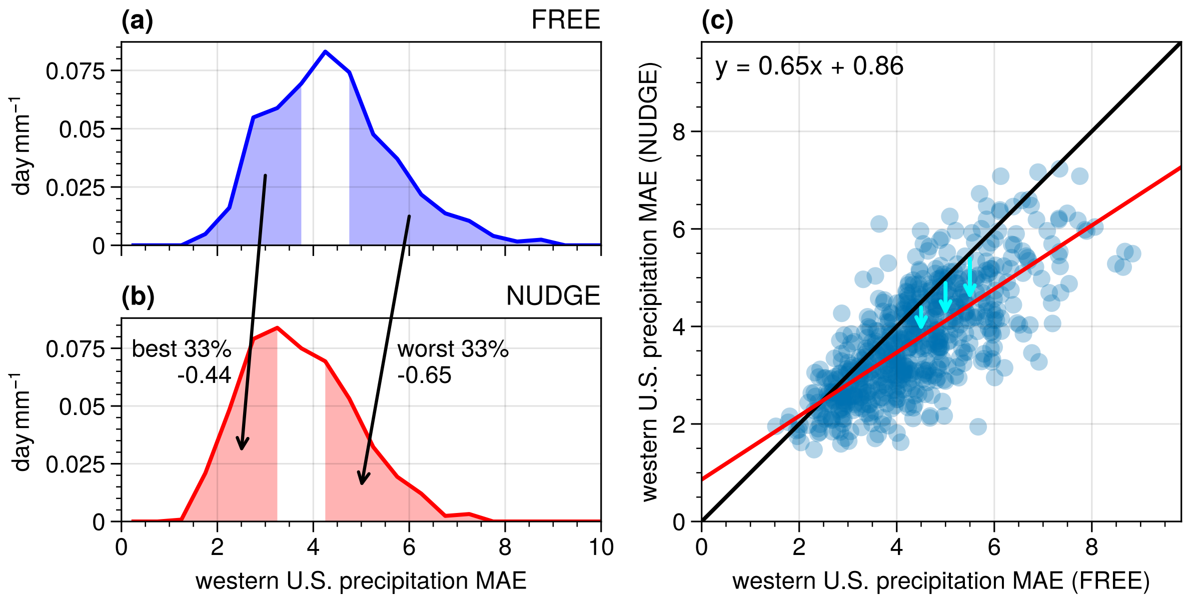

Figure A3.2. A histogram of the western U.S. precipitation MAE (mm day^{-1}) averaged over Weeks 3-4 in (a) FREE and in (b) NUDGE, and (c) a scatter plot of the two MAEs on individual days. For the histograms, the top and the bottom terciles in each run are shaded, and the arrows annotated with numbers indicate the improvements of each tercile between FREE and NUDGE. For the scatter plot, a linear regression of the data points is shown (red line; mathematical expression at the upper left corner) along with a reference one-to-one line (black), where the lengths of the cyan arrows demonstrate that the magnitudes of improvement are larger when the MAE in FREE is larger.

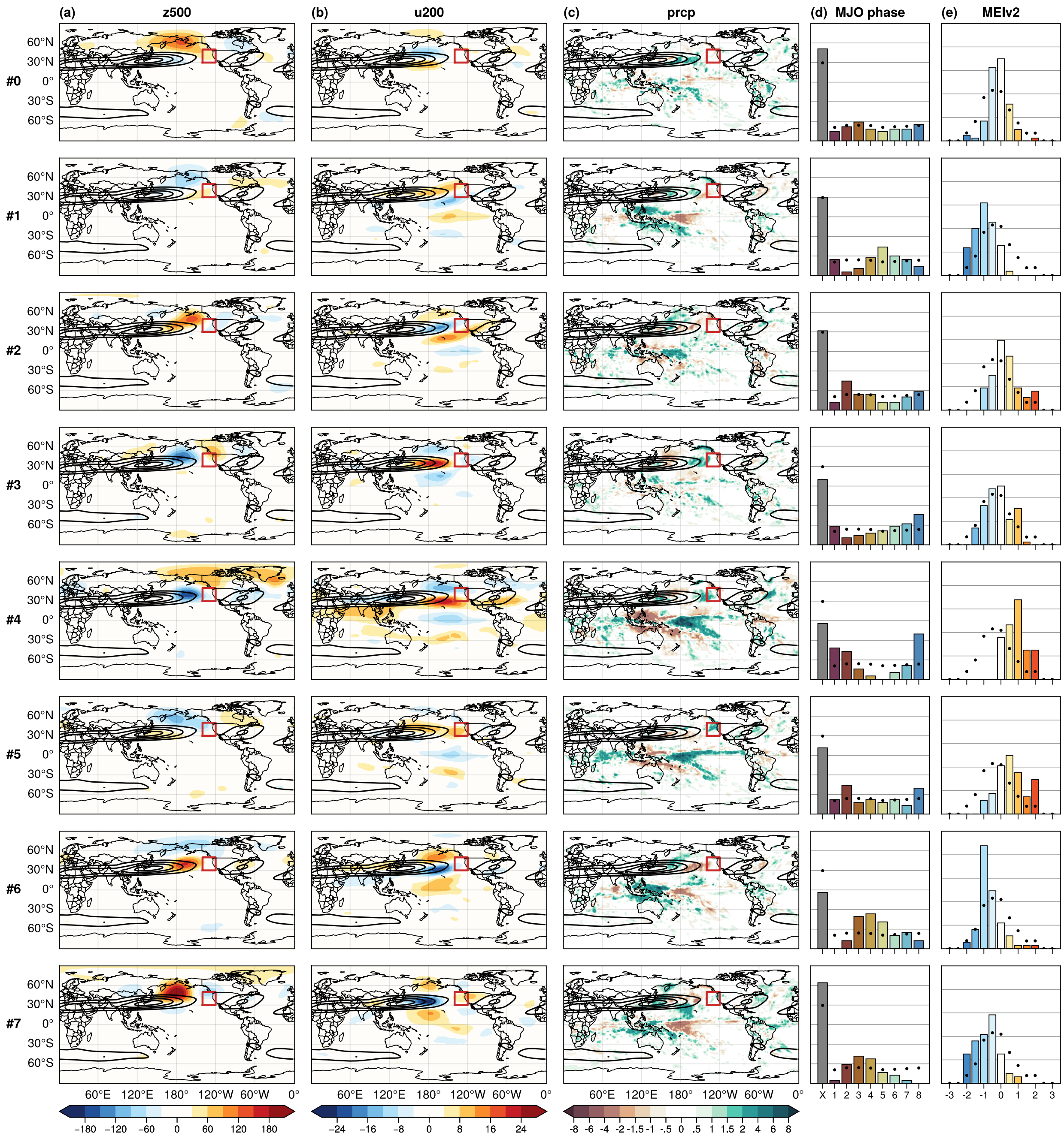

Figure A3.3. The composite anomaly from each cluster at Day 1: (a) z500 (m), (b) u200 (m s^{-1}), (c) precipitation (mm day^{-1}), and the distribution of (d) MJO phases, and (e) MEIv2. Each row represents a cluster. (d) and (e) are as constructed in a similar manner to **Figure 3.3c**. In (a), (b), and (c), the red boxes represent the western U.S. averaging region, and the black contours are the mean u200 from the extended boreal winter, with levels 30, 40, 50, 60, and 70 m s^{-1}.

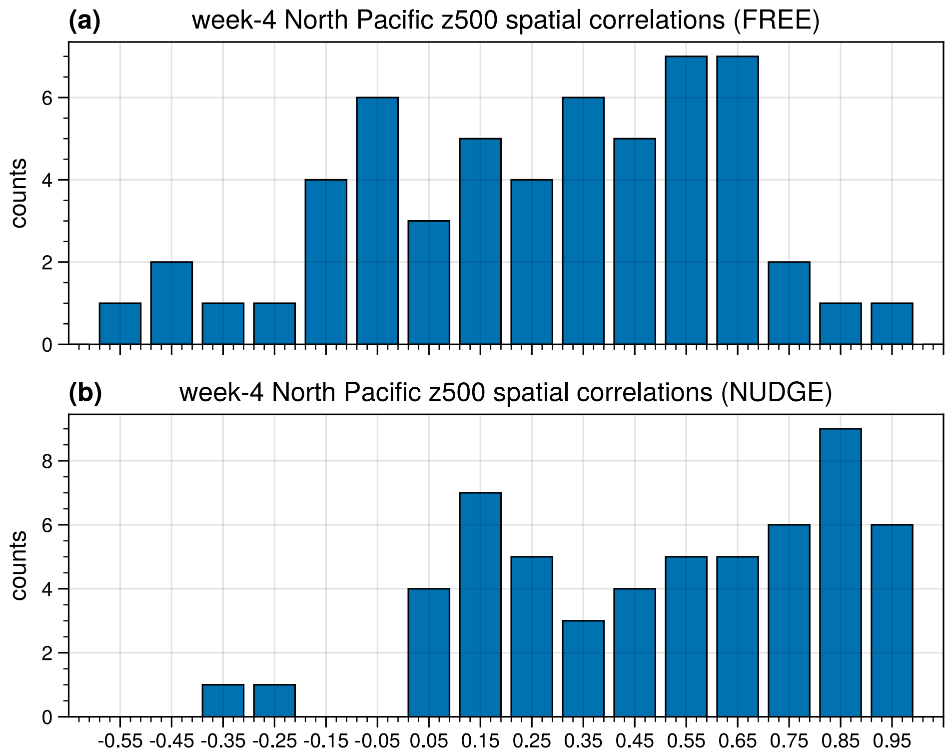

Figure A3.4. Histograms of North Pacific (20°N-70°N, 150°E-120°W) Week-4 z500 spatial correlation coefficients between REPLAY and (a) FREE and (b) NUDGE binned with interval 0.1.

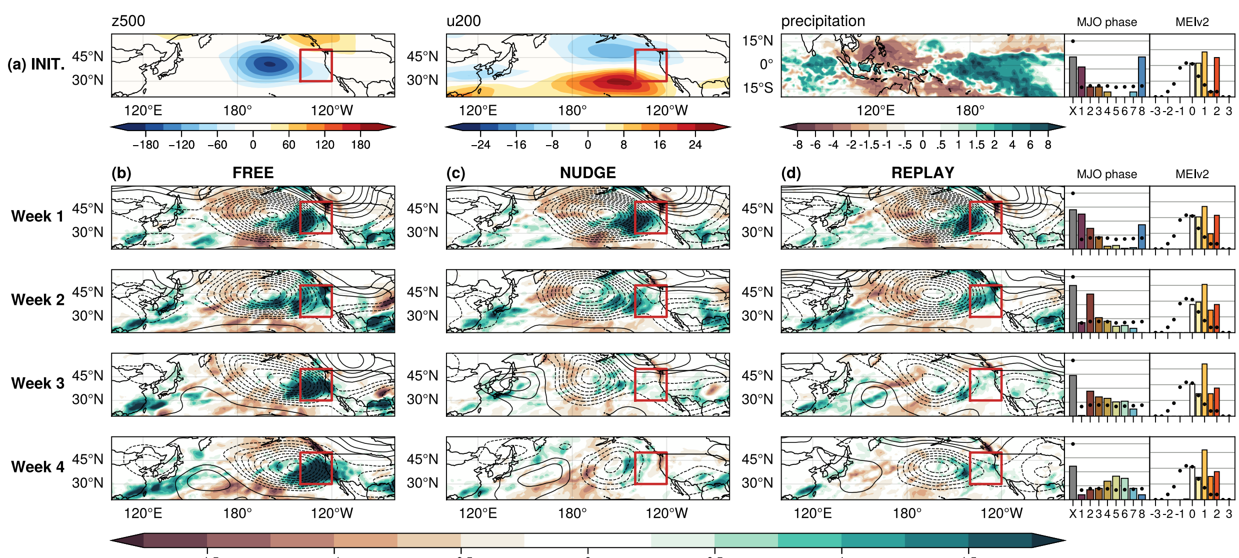

Figure A3.5. As **Figure 3.3**, but of the subset of hindcasts with the improvement greater than or equal to 1 mm day^{-1} from Cluster #4.

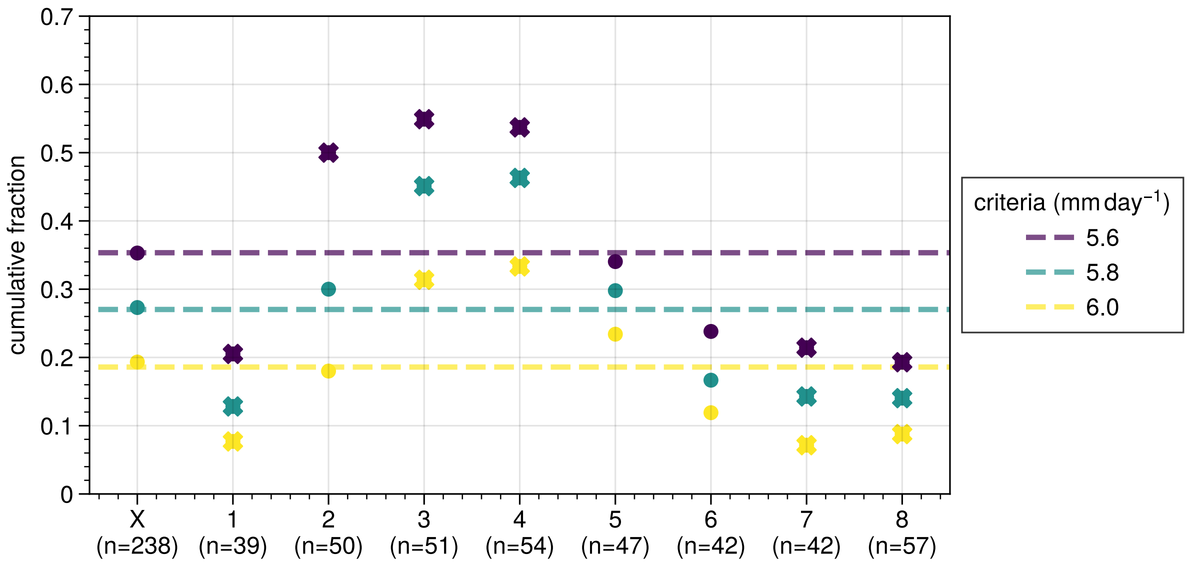

Figure A3.6. As **Figure 3.2b**, but showing the MAE reduction of Indo-Pacific warm pool region (10°S-10°N, 60°E-170°E) precipitation during weeks 1-2 as a function of MJO phase, where X indicates the non-MJO conditions.

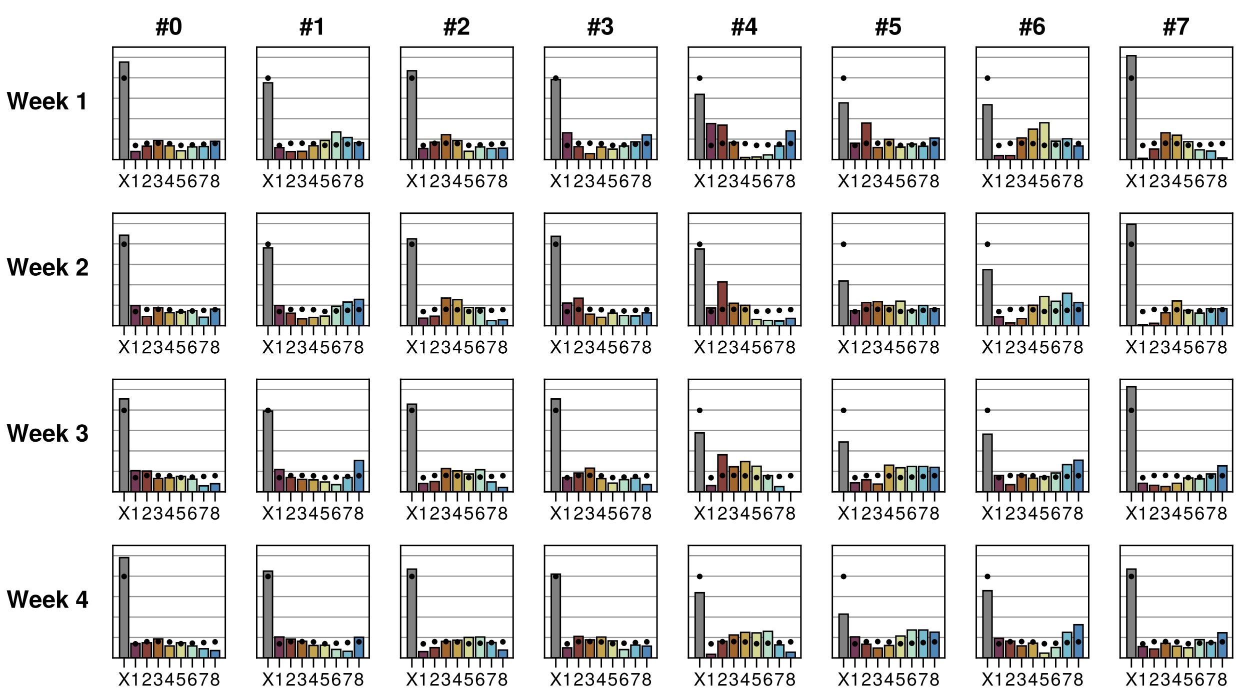

Figure A3.7. As the MJO panels in **Figure 3.3**, but showing the weekly distributions from all the clusters (columns).

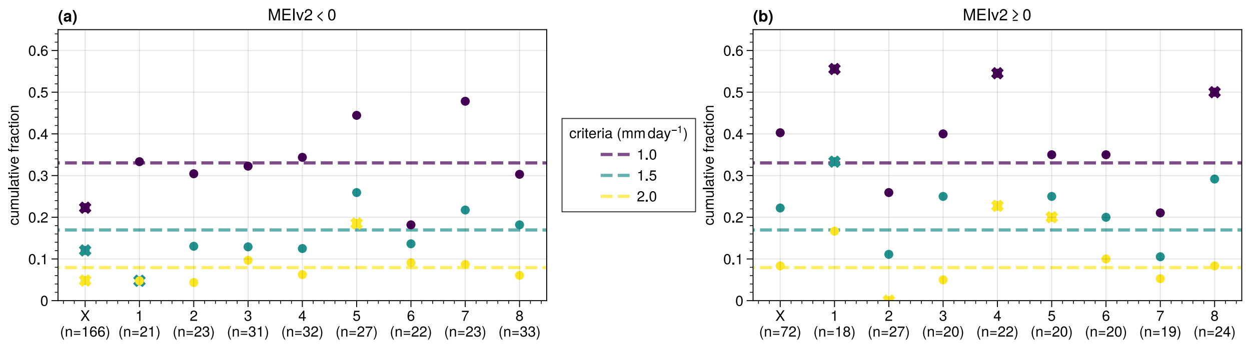

Figure A3.8. As in **Figure 3.2b**, but subsetting by MJO phases while (a) MEIv2 < 0, and while (b) MEIv2 ≥ 0, where X indicates the non-MJO conditions.

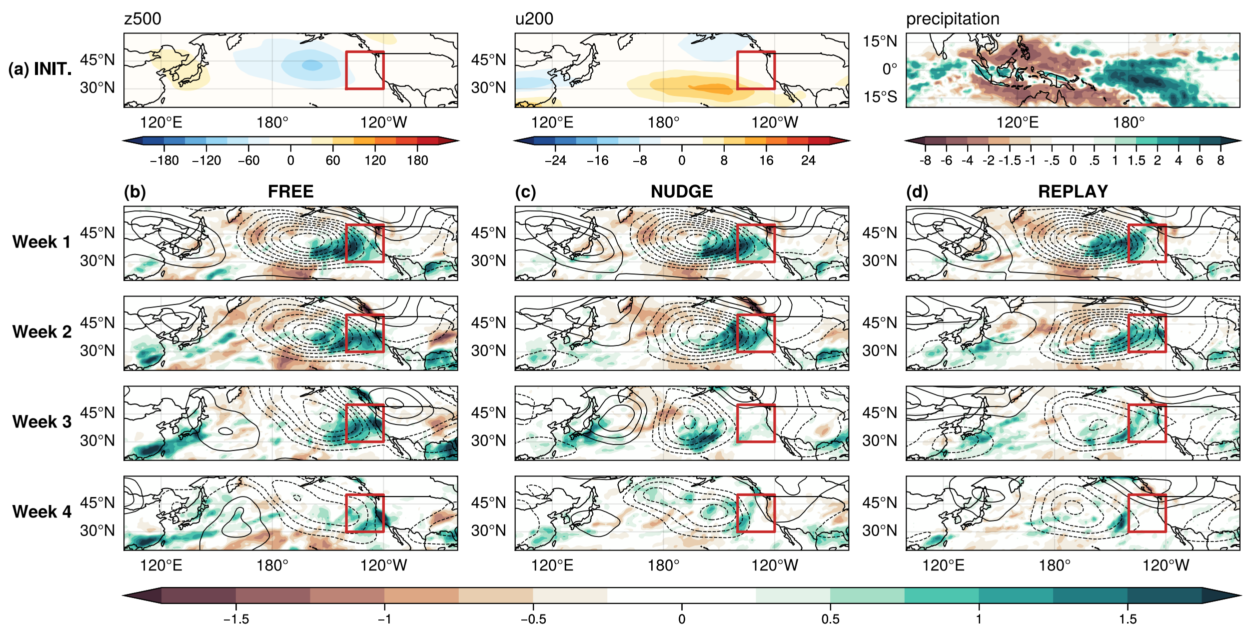

Figure A3.9. As **Figure 3.3** without showing the index distributions, but of the subset of hindcasts with MEIv2 ≥ 0 and MJO phases 1 and 8. The sample number of this subset is 42.